HAL
open science

# New stratigraphic and paleoenvironmental constraints on the Paleogene paleogeography of Western Amazonia

Michele Andriolli Custódio, Martin Roddaz, Roberto Ventura Santos, Pierre-Olivier Antoine, Laurent Marivaux, Narla S Stutz, Elton Luiz Dantas, Carlos Jaramillo, Mélanie Louterbach, Christian Hurtado, et al.

## ▶ To cite this version:

Michele Andriolli Custódio, Martin Roddaz, Roberto Ventura Santos, Pierre-Olivier Antoine, Laurent Marivaux, et al.. New stratigraphic and paleoenvironmental constraints on the Paleogene paleogeography of Western Amazonia. Journal of South American Earth Sciences, 2023, 124, pp.104256. 10.1016/j.jsames.2023.104256 . hal-04002216

**HAL Id: hal-04002216**

**https://hal.science/hal-04002216v1**

Submitted on 2 Aug 2023

**HAL** is a multi-disciplinary open access archive for the deposit and dissemination of scientific research documents, whether they are published or not. The documents may come from teaching and research institutions in France or abroad, or from public or private research centers.

L'archive ouverte pluridisciplinaire **HAL**, est destinée au dépôt et à la diffusion de documents scientifiques de niveau recherche, publiés ou non, émanant des établissements d'enseignement et de recherche français ou étrangers, des laboratoires publics ou privés.

*Journal of South American Earth Sciences* (Doi: https://doi.org/10.1016/j.jsames.2023.104256)

# New stratigraphic and paleoenvironmental constraints on the Paleogene paleogeography of Western Amazonia

Michele Andriolli Custódio [a, b, c, *], Martin Roddaz [a, c], Roberto Ventura Santos [a], Pierre-Olivier Antoine [d], Laurent Marivaux [d], Narla S. Stutz [d, e], Elton Luiz Dantas [a], Carlos Jaramillo [f], Mélanie Louterbach [g], Christian Hurtado [h], Guilherme Oliveira Gonçalves [a]

[a] *Laboratório de Geocronologia, Instituto de Geociências, Universidade de Brasília, Brasília, DF 70910-000, Brazil*

[b] *Programa de Pós-Graduação em Geociências, Universidade Federal do Amazonas, CEP: 69.077-000, Manaus, AM, Brazil*

[c] *Géosciences-Environnement Toulouse, Université de Toulouse, UPS (SVT-OMP), CNRS, IRD, 14 Avenue Édouard Belin, 31400 Toulouse, France*

[d] *Institut des Sciences de l'Évolution de Montpellier, Univ Montpellier, CNRS, IRD, Place Eugène Bataillon, 34095, Montpellier, France*

[e] *Programa de Pós-Graduação em Geociências, Universidade Federal do Rio Grande do Sul (PPGGEO UFRGS). Av. Bento Gonçalves, 9500, 91501-970, Porto Alegre,*
*Rio Grande do Sul, Brazil*

[f] *Smithsonian Tropical Research Institute, Roosevelt Avenue, Building 401 Balboa, Ancon, Panama City, Panama*

[g] *Harvard Graduate School of Design, Department of Landscape Architecture, 48 Quincy Street, MA 02138 Cambridge, USA*

[h] *Universidad Nacional Mayor de San Marcos, Av. Venezuela Cda. 34 S/n Lima-Cercado, Lima, Peru*

***Keywords:*** *Zircon, U–Pb dating, C and O isotopes, Shallow marine deposits, Northern Peru, Paleogeography*

* Corresponding author: Programa de PósGraduação em Geociências, Universidade Federal do Amazonas, CEP 69.077-000, Manaus, AM, Brazil
*E-mail address:* mi.andriolli@gmail.com (M.A. Custódio).

## Abstract

The rise of the Andes and the associated propagation of the retroarc foreland basin during the Mesozoic Cenozoic in western South America shaped the paleogeography and paleoenvironmental settings of Western Amazonia. Much attention has been paid to the Neogene evolution of the Amazonian Basin, but few studies have investigated in detail the paleoenvironments of Western Amazonia during the Paleogene. We present a multi-proxy study that includes new biostratigraphic and paleontologic data, the interpretation of depositional environments and zircon U–Pb data from the Upper Cretaceous-Paleogene sedimentary sequence exposed in the Huallaga Basin (northern Peru). The biostratigraphic dating suggests that the lower part of the sequence is Maastrichtian in age. The maximum depositional age and maximum likelihood age according to the U–Pb zircon dating of Paleogene sedimentary rocks indicate Lutetian to Bartonian ages (from 43.5 ± 0.64 Ma to 37.6 ± 0.85 Ma). These results reveal a hiatus in the depositional record during Paleocene time. Two depositional systems can be distinguished: a lacustrine system composed of red mudrocks interbedded with thick sandstone layers and carbonate beds, and a siliciclastic tide-dominated system composed of fine- to medium-grained sandstones associated with tidal bundles, reactivation surfaces and heterolithic stratifications. However, the carbon and oxygen stable isotope values in carbonates tend to characterize a freshwater system, with a transition to brackish conditions toward the upper part of the section (Bartonian), thereby suggesting the presence of an estuary system. Finally, we suggest that the Bartonian shallow marine incursion recorded in the Huallaga Basin occurred from the north through the Caribbean Sea, and that it might have played a role in regional biodiversity patterns in the Paleogene.

## 1. Introduction

Precise knowledge of the geological evolution of Amazonian landscapes and ecosystems is a prerequisite for understanding species diversification in this vast area today biodiversity seems to be deeply rooted in the pre-Quaternary (Hoorn et al., 2010b, and the references therein). The uplift of the Andes reconfigured drainage patterns, involved a vast influx of sediments into the Amazonian basins (Fig. 1) (e.g. Roddaz et al., 2010, 2005a), and caused shallow marine incursions in Western Amazonia (Jaramillo et al., 2017; Boonstra et al., 2015; Hovikoski et al., 2010).

Recently, much attention has been paid to the Neogene paleogeography of the Amazonian basins, especially to the timing of the modern transcontinental Amazon River (Hoorn et al., 2017, van Soelen et al., 2017; Eakin et al., 2014; Gorini et al., 2014; Sacek, 2014; Shephard et al., 2010; Figueiredo et al., 2009). Attention has also been given to the Neogene paleogeography of Western Amazonia (Hoorn et al., 2010a) and the number and nature of marine incursions that affected this area during the Miocene (i.e., the Pebas megawetland system) (Jaramillo et al., 2017; Antoine et al., 2016; Boonstra et al., 2015; Hovikoski et al., 2010; Hoorn, 1993). However, surface uplift driven by the tectonism and denudation of the present-day Amazonian Andes area started much earlier, as recorded in the Upper Maastrichtian-Paleocene deposits (Hurtado et al., 2018; Louterbach et al., 2018b).

In comparison with the Neogene period, the Paleogene paleoenvironmental changes of Western Amazonian basins have still a poorly documented and poorly dated stratigraphic record. Notable exceptions are the detailed studies of Antoine et al. (2016) and Louterbach et al. (2018b). In the Late Cretaceous (Middle Campanian and Late Maastrichtian), the sedimentary record of the Ecuadorian and northern Peruvian parts of the Western Amazonian Basin (i.e., the Marañón Basin) (Fig. 1) indicates thick transgressive-regressive sequences alternating between fluvial-marine paleoenvironments controlled by eustatic processes (Zamora and Gil, 2018). It is unclear whether or not these conditions prevailed during the Paleogene and how the onset of the Andean uplift affected the landscape and paleoenvironment of Western Amazonia.

Two shallow marine transgressions that occurred during the Paleogene are currently documented in Western Amazonia. The oldest one is a Late Paleocene shallow marine transgression characterized by estuarine and bay paleoenvironments (Louterbach et al., 2014). This latter event has only been documented in the southern part of the Amazonian retroarc foreland basin (Madre de Dios Basin, Peru) (Fig. 1), and the entrance of this transgression remain unclear (Louterbach et al., 2014). The second transgression is a Middle to Late Eocene shallow marine incursion known as the "Pozo" embayment or transgression, which flooded the northern part of the Amazonian retroarc foreland basins

from the Gulf of Guayaquil or the Caribbean Sea (Roddaz et al., 2010; Santos et al., 2008; Christophoul et al., 2002; Antoine et al., 2016). However, the southwestern margin extension of this Pozo embayment needs to be better constrained. Hence, documenting Paleogene paleo- environments in other parts of the Western Amazonian Basin may contribute to resolving these issues.

The Cretaceous–Cenozoic sedimentary infilling of the Huallaga Basin (Calderón et al., 2017a; Eude et al., 2015; Hermoza et al., 2005) has the unique potential to have recorded the Cretaceous–Paleogene paleo- environmental evolution of the northern part of Western Amazonia as previous studies show major changes in the sedimentary provenance between the late Cretaceous and the Paleocene (Hurtado et al., 2018). The aim of this work is to characterize the paleoenvironmental evolution of the Huallaga Basin during the late Cretaceous-Paleogene time window, as a key element for unraveling the Andes – Amazon sedimentary evolution.

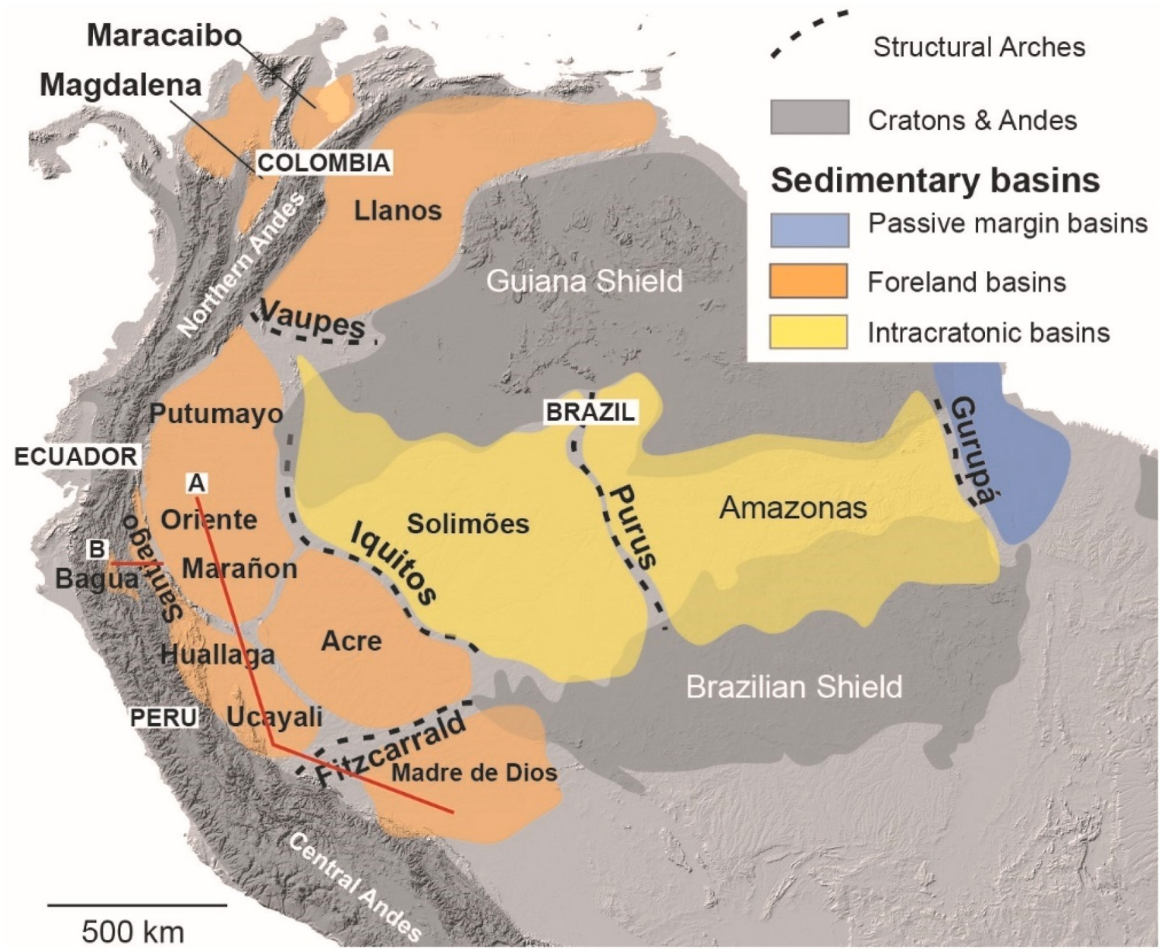


**Fig. 1.** Map of the geographic extent of the major morphotectonic provinces of the northern South America, from west to east, the retroarc foreland basins (Colombia, Ecuador and Peru countries), the intracratonic and passive margin basins (Brazil), partially bounded by structural arches (dashed lines). Northern and Southern Amazon Craton are represented by the Guiana and Brazilian shields, respectively (modified and compiled from Albert et al., 2018; Moreno et al., 2020; Roddaz et al., 2010). The red lines indicate the location of Fig. 3 A and 3 B.

Our contribution comprises the first detailed stratigraphic analysis of the late Cretaceous–Paleogene sedimentary section, based on new multi-proxy analyses including sedimentological facies, biostratigraphy (palynostratigraphy and vertebrate biochronology), stable isotopes (C, O) in carbonates, and maximum depositional ages based on the U–Pb dating of detrital zircons.

## 2. Geological background

### *2.1. Tectonic setting and stratigraphy of the Huallaga Basin*

The north-south trending Huallaga Basin (Fig. 2) is currently 400 km long with a maximum width of 100 km (Hermoza et al., 2005), and it is part of the northern Peruvian Subandean Zone. It consists of the wedge-top depozone (DeCelles and Giles, 1996) of the North Amazonian retroarc foreland basin (Espurt et al., 2010, 2007; Roddaz et al., 2005b) that formed in response to the tectonic loading of the Andes (Roddaz et al., 2010). To the east, the Huallaga Basin is separated from the Marañón Basin by the Cushabatay High and Chazuta Thrust; the latter corresponds to the thrust front of the Subandean Zone (SAZ) (Fig. 2) (Calderón et al., 2017a; Hermoza et al., 2005). To the west, the Huallaga Basin is delimited by the Eastern Cordillera (Fig. 2). A sequential restoration based on low-temperature thermochronology and balanced cross-sections suggests that the Eastern Cordillera started to be uplifted between ca. 30 and 24 Ma, which caused thrusts to propagate over a regional detachment level located in the Upper Triassic evaporites (Carrillo et al., 2021; Calderón et al., 2017a, 2017b; Eude et al., 2015). The Cretaceous tectonic configuration of the Huallaga Basin is less constrained. The most recent model suggests that it could be part of a passive margin (Zamora and Gil, 2018) that received sediments from the Amazonian Craton (Hurtado et al., 2018).

The Cretaceous sequences of the Huallaga Basin comprise Albian to Maastrichtian fluvial to shallow marine successions of sandstones, shales and limestones (Cushabatay-Raya, Agua Caliente-Chonta, and Vivian-Cachiyacu-Huchpayacu formations) (Baby et al., 2018; Calderón et al., 2017a, 2017b) (Fig. 3). The Albian–Maastrichtian sedimentary rocks of the Huallaga Basin have εNd (0) values (−16.8 to −18.6) consistent with a cratonic source, and a U–Pb zircon age distribution dominated by the easternmost Brazilian Shield terranes (Hurtado et al., 2018).

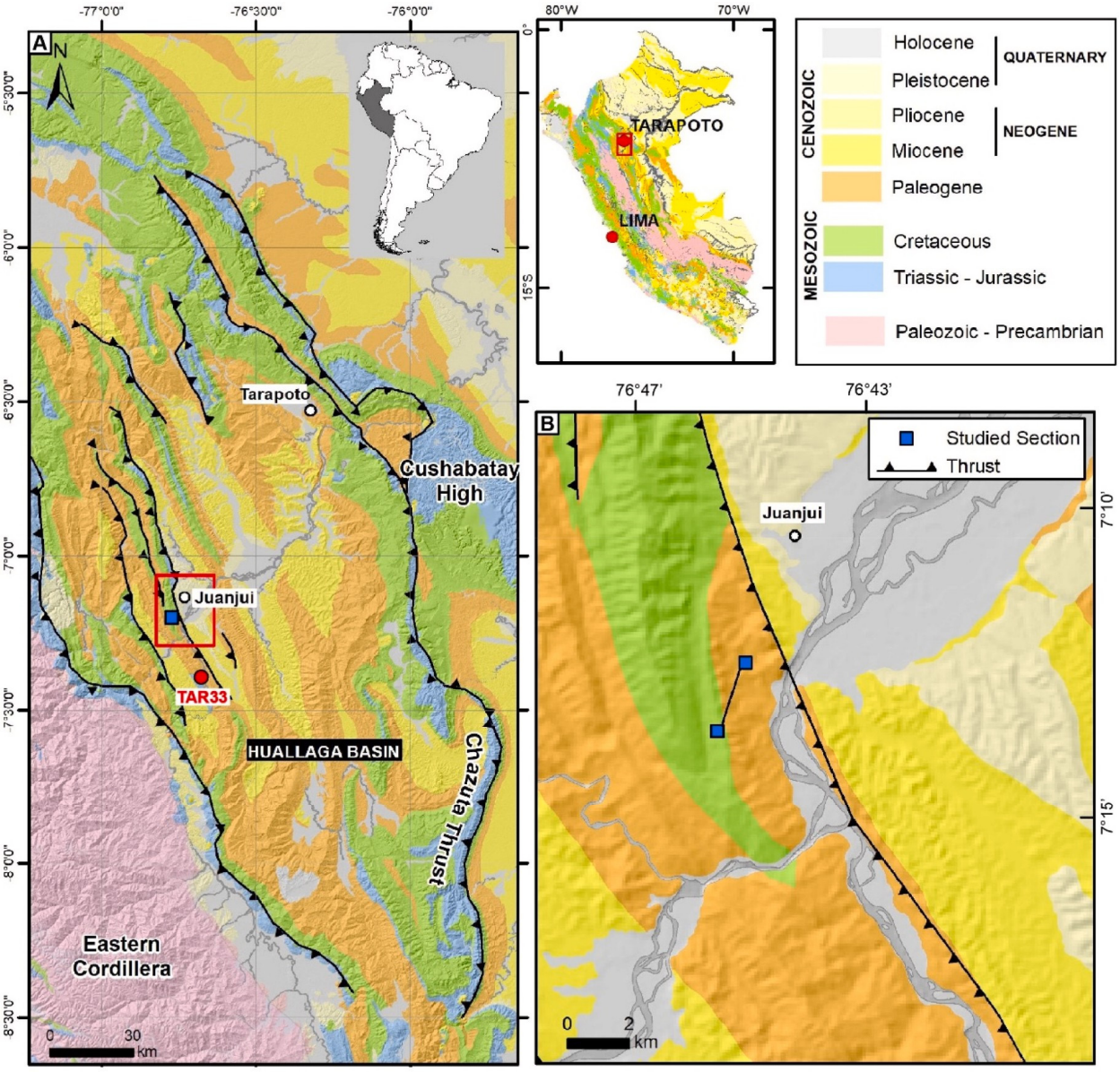


**Fig. 2.** Geological map of the studied area modified from the INGEMMET Geological Map of Peru available at http://geocatmin.ingemmet.gob.pe/geocatmin/. A) Regional geologic map of the Huallaga Basin, which is separated to the west from the Eastern Cordillera and limited, to east, from Marañón Basin by the Chazuta thrust and the Cushabatay High. The red rectangle indicates the location of the Juanjuí stratigraphic section. Location of the large dinosaur tracks is represented by TAR-33; B) Detailed geological map showing the Mesozoic-Cenozoic geological contacts and the stratigraphic position of the Juanjui studied section.

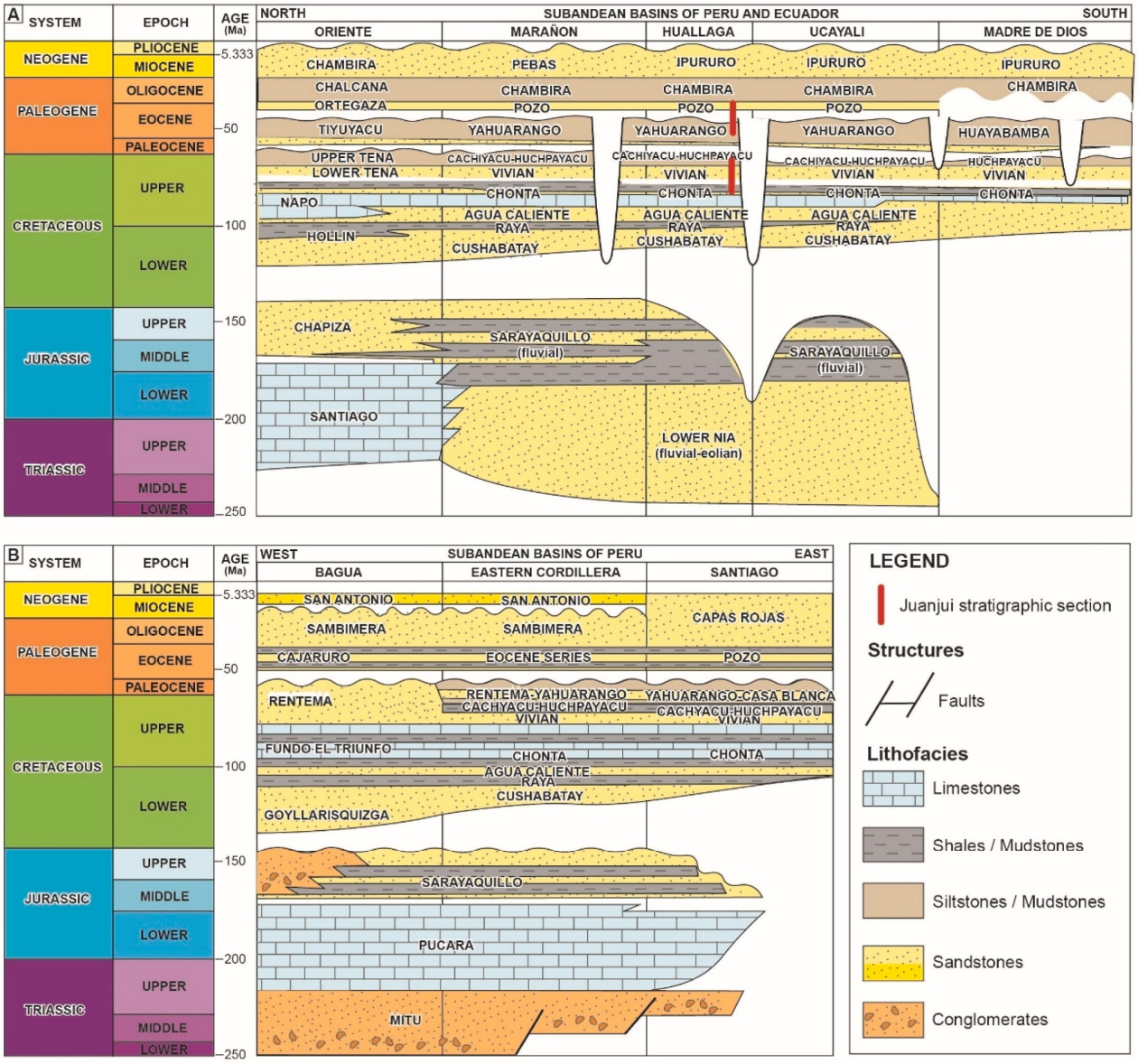


**Fig. 3.** Comparative chronostratigraphic diagram showing the stratigraphic nomenclature, age, lithology, tectonic setting, and stratigraphic discontinuities for (A) the Ecuadorian and Peruvian Subandean Amazonian basins and (B) Peruvian Amazonian foreland basins. The chronostratigraphic diagram (A) was constructed based on Baby et al. (2013); Calvès et al. (2018); Roddaz et al. (2010), Hurtado et al. (2018); Hermoza et al. (2005); Louterbach et al. (2014), and Calderón et al. (2017a, 2017b). The chronostratigraphic diagram (B) is based on Moreno et al. (2020, 2022) and George et al. (2019).

The Cenozoic stratigraphy of the Huallaga Basin still needs to be better constrained. Calderón et al. (2017a) proposed that the Paleocene–lower Eocene sedimentary sequence started with the fluvial and tidal sandstones of the Casa Blanca Formation (Fm.), whereas other authors suggested that the Cenozoic sedimentary sequences started with the Paleogene fluvial sedimentary rocks of the Yahuarango Fm. (Hurtado et al., 2018; Roddaz et al., 2010; Hermoza et al., 2005; Gutiérrez, 1982; Kummel, 1948). According to Hurtado et al. (2018), the Paleogene sedimentary rocks of the Yahuarango Fm. have an Andean provenance, with εNd (0) values ranging between −5.6 and −12.0, and up to 16% of U–Pb zircon ages are derived from the Andean volcanic arc.

*2.2. Stratigraphy of other Western Amazonian basins*

The Amazonian retroarc foreland basins experienced similar geological evolutions until the Pliocene uplift of the Fitzcarrald Arch (Fig. 1 and, 3) (Roddaz et al., 2010; Espurt et al., 2010). An extensional phase in a back-arc basin setting controlled the deposition of the mixed clastic and volcanic deposits of the Triassic Mitu group (George et al., 2019; Calderón et al., 2017b), as recorded in the Bagua Basin, the Eastern Cordillera of Peru and the Santiago Basin (Fig. 3). Farther southeast (Marañón-Huallaga-Ucayali basins), a regional extensional basin created due to post-extensional thermal subsidence drove the deposition of the Triassic-Jurassic eolian-fluvial deposits of the Lower Nia Fm. (Calderón et al., 2017a, 2017b). These deposits grade laterally into the shallow marine carbonates of the post-rift Pucara Group and the Sarayaquillo fluvial sequence, as recorded in the Ecuadorian and Peruvian basins (George et al., 2019; Hurtado et al., 2018; Calderón et al., 2017b) (Fig. 3A and B). The Late Jurassic to Early Cretaceous are marked by a widespread sedimentary hiatus (145-120 Ma) (Hurtado et al., 2018; Calderón et al., 2017b) (Fig. 3A and B). Overlying this erosional unconformity, the Cretaceous sedimentary rocks comprised Albian to Maastrichtian fluvial to shallow marine deposits, mainly represented by the Goyallarisquizga, Cushabatay-Raya; Agua Caliente-Chonta, and Vivian-Cachiyacu-Huchpayacu formations (Fig. 3A and B).

From the Late Cretaceous to the Early Paleogene, the Andean shortening started to control the configuration of the Western Amazonian basins (Horton, 2018; Hurtado et al., 2018; Louterbach et al., 2014, 2017; Calderón et al., 2017b; Hermoza et al., 2005). The Cenozoic retroarc foreland infill comprises the fluvial and lacustrine siltstones/mudstones of the Paleogene Yahuarango Fm. (Marañon-Huallaga-Ucayali basins) (Hurtado et al., 2018; Roddaz et al., 2010; Hermoza et al., 2005; Gutierrez, 1982; Kummel, 1948), which can be correlated with the Tiyuyacu (Oriente Basin) (Baby et al., 2013) and Huayabamba formations (Madre de Dios Basin) (Louterbach et al., 2014). These formations can be correlated with the Paleocene-lower Eocene braided fluvial deposits of the Rentema Fm. in the Bagua Basin (Moreno et al., 2022, 2020) (Fig. 3B).

These formations are separated from the youngest formations by a middle Eocene regional unconformity recorded in the Ecuadorian and Peruvian retroarc foreland basins (Fig. 3) (Roddaz et al., 2010; Christophoul et al., 2002). The shallow marine deposits of the middle Eocene-Oligocene Pozo Fm. are recorded in the Santiago, Marañón, Huallaga and Ucayali basins. The Pozo Fm. can be correlated to the north with the Ortegaza Fm. (Oriente Basin) (Baby et al., 2013) and to the west with the Eocene Series (Eastern Cordillera) and the fluvio-lacustrine Cajaruro Fm. (Bagua basin) (Moreno et al., 2022, 2020) (Fig. 3A and B). It is overlaid by the Upper Oligocene-Lower Miocene fluvial deposits of the Chambira Fm. in the Peruvian retroarc foreland basins (Antoine et al., 2016) and by the Chalcana Fm. in the Ecuadorian Oriente retroarc foreland basin (Baby et al., 2013). These formations can be correlated with the Upper Eocene-middle Miocene meandering deposits of the Sambimera Fm. in the Bagua Basin (Moreno et al., 2022, 2020) and Eastern Cordillera, and the Capas Rojas Fm. in the Santiago Basin (George et al., 2019) (Fig. 3B). Finally, the Neogene sedimentary deposits are characterized by the fluvial deposits of the Ipururo, Chambira and San Antonio formations in the Bagua Basin, Eastern Cordillera, Huallaga, Ucayali, Madre de Dios basins (Moreno et al., 2022, 2020; George et al., 2019; Calderón et al., 2017b; Hermoza et al., 2005) (Fig. 3A and B). These deposits can be correlated with those of the Pebas Fm. that belong to the Pebas megawetland system (Hoorn et al., 2010a; Jaramillo et al., 2017; Antoine et al., 2016; Boonstra et al., 2015; Hovikoski et al., 2010; Hoorn, 1993) in the Marañón Basin.

## 3. Materials and methods

### *3.1. Sedimentology*

We studied in detail one Mesozoic–Cenozoic section, the Juanjuí section (Fig. 4). The outcrops investigated in this study crop out along the 5 N national road close to the Huallaga River and the city of Juanjuí (see Fig. 2 for the location and Supplementary Material S1 for the coordinates). To better understand the depositional environment, we measured and described several outcrops along the Juanjuí stratigraphic section. We described the clastic facies in terms of their lithology, geometry, sedimentary structures and paleontological content (Miall, 2006, 1978). The chemical facies (microfacies) were described using Dunham's (1962) classification, which considers the abundances of carbonates, mud and grains; this helps to better constrain the formation process and/or paleoenvironmental conditions. The most commonly used criteria are the depositional texture and fabric, as well as qualitative and quantitative compositional data (Flügel, 2010). As pointed out by Walker (1992), most classifications for carbonates were originally conceptualized for marine systems, but they have also been used for lacustrine deposits

with some adjustments. The carbonate thin sections were prepared at the *Laboratório de Laminação* (LABLAM) of the *Universidade de Brasília* (UnB). Thirteen sedimentary facies have been identified (Table 1).

### *3.2. Stable isotopes*

Forty-six samples of limestones and sandstones in a carbonate matrix were collected along the Juanjuí stratigraphic section (Fig. 4). The abbreviations HUA (Huallaga) and JUA (Juanjuí) are used to refer to the samples obtained during field work performed in September 2017 and August 2019, respectively. The carbon and oxygen isotopic compositions are shown in Supplementary Material Table S2.

The samples were analyzed at the Geochronology and Isotope Geochemistry Laboratory of the University of Brasília (LEGGA) on a Delta V Plus mass spectrometer connected to a Gas Bench II apparatus. The samples reacted with $H_3PO_4$ at a temperature of 72 °C after the flask was flushed with helium. Stable isotope results are reported in delta notation relative to the Vienna Pee Dee Belemnite (V-PDB) reference standard, and they were calibrated against the NBS 18 ($\delta^{13}C_{V\text{-}PDB}$ = –5.01‰ and $\delta^{18}O_{V\text{-}PDB}$ = –23.2‰) and NBS 19 ($\delta^{13}C_{V\text{-}PDB}$ = 1.95‰ and $\delta^{18}O_{V\text{-}PDB}$ = –2.20‰) reference materials. A linear regression of the standard results followed by correction of the sample data, were performed to account for instrumental bias. To avoid any diagenetic biases, we selected only well-preserved samples.

The isotopic composition of carbon and oxygen in a sample was expressed by dividing the isotopic ratio (R) measured in the sample by the isotopic ratio of a standard (V-PDB) using the δ notation; the isotopic composition is expressed in parts per thousand (‰). $\delta^{13}C$ and $\delta^{18}O$ were obtained as follows: $\delta^{13}C_{(sample)} = [(R_{sample}/R_{V\text{-}PDB}) - 1] * 10^3$, and $\delta^{18}O_{(sample)} = [(R_{sample}/R_{V\text{-}PDB}) - 1] * 10^3$, respectively (Guiguer et al., 2003).

### *3.3. Palynological analysis*

The palynological samples were prepared at the Universidad de Caldas following the standard palynological processing method pro- posed by Traverse (2007). Carbonates and silicates were removed by digesting the samples in HCl and HF for 12 and 24 h, respectively. After acid digestion, the samples were neutralized through repeated dilution with distilled water and decanting. The remaining residue was initially sieved with a 250 µm mesh; this was followed by sieving through a 10 µm mesh. This residue was cleaned in an ultrasonic equipment for 15 s and the organic residue was concentrated by centrifugation, followed by the mounting of a first cover slide in a solution of polyvinyl alcohol. Part of the residue

was oxidized in nitric acid for 2–3 min, and a second slide was mounted. The slides were sealed with Canadian balsam. A Nikon i80 at the Smithsonian Tropical Research Institute was used to scan the slides. The examination and description of the palynological material were carried out using a 100x Nikon oil immersion planapochromatic objective. The identification of the palynomorphs was performed through a comparison with photographs and descriptions of Cretaceous and Paleocene material published for northern South America that are compiled in an online database (Jaramillo and Rueda, 2021). The palynological zonation of Jaramillo et al. (2011) and the biostratigraphic analysis of Carvalho et al. (2021) and De La Parra et al. (2021) were used to assess the age of the samples.

*3.4. U–Pb ages*

Zircon grains were obtained from three samples of medium-grained sandstones collected along the Juanjuí section (JUA 8A/19, 11 and 14; Fig. 4, S1 and S3–S5). For U–Pb analyses, each sample was prepared and analyzed at the Geochronology and Isotope Geochemistry Laboratory (LEGGA) of the University of Brasília (UnB). The sample preparation process included crushing rock samples, which was followed by heavy mineral separation by panning. Additionally, another separation was performed based on the magnetic properties of the minerals using the Frantz Isodynamic Magnetic Separator. A random selection of the zircon grains was handpicked (~150 grains per sample) under a stereomicroscope, mounted on adhesive tape, enclosed in a 9-mm-diameter plastic ring placed on the tape around the zircons and filled with epoxy resin. Finally, the zircon grains were polished to expose their centers (Gehrels, 2014; Bühn et al., 2009; Gehrels et al., 2008). The mounts with zircon grains were imaged by a scanning electron microscope (SEM) and back-scattered electron (BSE) detector to identify morphological features and internal structures and to provide a base map for recording laser spot locations. The masses of interest were measured on a Thermo Finningan Element XR high-resolution single-collector sector field Inductively Coupled Plasma Mass Spectrometry (ICP-MS) coupled to a 193 nm Iridia Excimer (ArF) laser ablation system. The laser ablation system is equipped with a cobalt dual-volume chamber. The mass spectrometer was tuned to improve U and Pb sensitivity while minimizing oxide production prior to each analytical session. Each analysis consisted of 10 s of background measurement followed by 20 s of sample acquisition. Each mass (202, 204, 206, 208, 232, 238) was measured using the triple detection mode (SEM  Faraday) by sweeping the electrostatic sector on each mass. Each sweep lasted 82 ms, resulting in over 800 scans for each ablation. Laser conditions included a spot diameter of 25 µm, 20 Hz and 2.0 J cm-2. The raw data were processed on Iolite 4.0 (Paton et al., 2011) as a time-resolved signal and individual signal inspection was done with the assistance of VizualAge (Petrus and Kamber, 2012). Data correction included blank

subtraction, Laser Induced Elemental Fractionation (LIEF) correction using an exponential plus linear model and normalization using the GJ-1 zircon (Jackson et al., 2004) and 91,500 zircons (Wiedenbeck et al., 1995). Excess variance on the primary calibrant was propagated on each analytical point. A systematic uncertainty of *ca.* 1% is propagated on each final age. No common lead correction was applied. The ages uncertainties are quoted at 2 sigma (2σ) confidence level.

The data reduction of the U–Pb isotopic results for detrital zircons was conducted using Iolite 4.0 and followed the procedures of Paton et al. (2011). Details regarding the LA-ICP-MS U–Th–Pb dating of the analyzed samples at the LEGGA can be found in Tables S3–S6 (supplementary dataset).

For the three analyzed samples, we calculated a maximum depositional age using two different statistical methods, the "maximum depositional age' (MDA) and "maximum likelihood age' (MLA) (Table S6). The MDA was calculated as the weighted mean average of the overlapped analyses of the three youngest zircons and the associated 2σ uncertainty of this cluster (YC2σ[3+]; Sharman and Malkowski, 2020; Sharman et al., 2018; Dickinson and Gehrels, 2009). The MLA is a statistical model that assumes that the zircon U–Pb ages are defined as a two-component mixture in which a "fraction of the population is derived from a discrete minimum age peak and the remaining grains follow a (log)normal distribution" (Vermeesch, 2021; Galbraith, 2005; Galbraith and Laslett, 1993). The MLA was calculated using IsoplotR (Vermeesch, 2021, 2018).

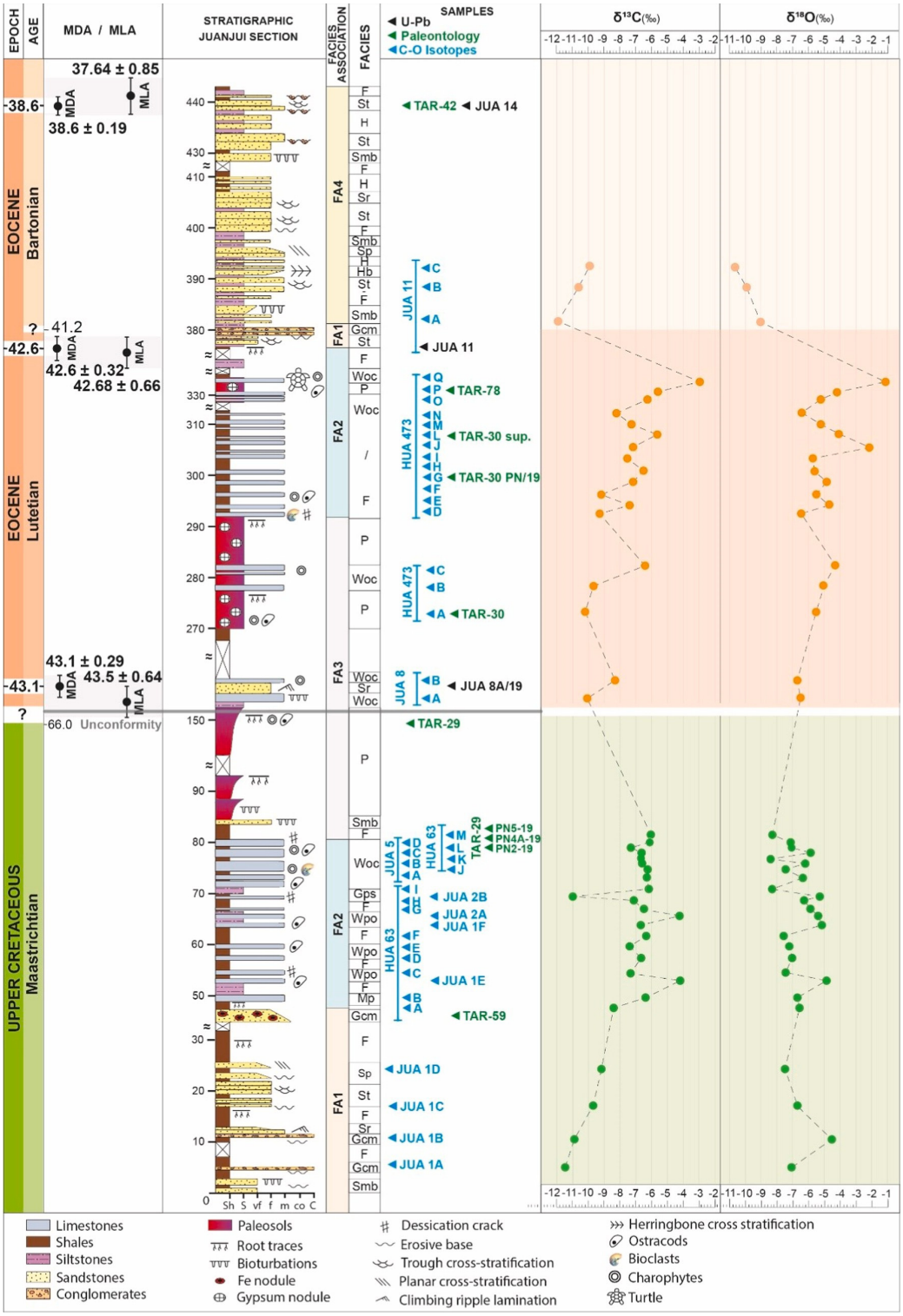


**Fig. 4.** Synthetic Juanjuí stratigraphic section through the late Cretaceous (Maastrichtian) to late middle Eocene (Bartonian) at the Huallaga Basin, constructed from field observations, with location of the analyzed samples for C–O isotopic compositions, paleontological content (biostratigraphic constraints) and U–Pb zircon dating. Siliciclastic facies: massive clast-supported conglomerate (Gcm); trough cross-stratified sandstone (St), planar cross-stratified sandstone (Sp), climbing ripple cross-laminated sandstone (Sr), bioturbated sandstone (Smb), heterolithic facies (H), herringbone cross-stratified sandstone (Hb), fines (F) and paleosol (P). Carbonate microfacies: peloidal mudstone (Mp); wackestone with peloids and ostracods (Wpo); wackestone with ostracods and charophytes (Woc); and pisolitic grainstone (Gps). FA= Facies association. See text and Table 1 for details.

**Table 1**
Summary of the descriptions and interpretations of each sedimentary siliciclastic facies and carbonate microfacies.

| Facies/ Microfacies | Lithology and Texture | Sedimentary Structures | Paleontological content | Ichnology | Thickness (m) | Other characteristics/ Geometries | Interpretation |
|---|---|---|---|---|---|---|---|
| **Siliciclastic facies** | | | | | | | |
| Gcm Massive clast-supported conglomerate | Rounded- to sub-rounded mud-clasts (monomictic conglomerates), with cm-dm size (3–15 cm), scattered in the bed. Matrix composed by medium- to coarse-grained arkosik sandstones, with scattered subrounded granules and pebbles (milky quartz pebbles). Poorly-defined fining-upward trend; very poor sorting | Massive | No fossils | No trace fossils | 0.3–0.5 | Discontinuous and cuneiform beds, marked by concave-up bases | This deposits could be referred as filling of a channel lag deposits, under high sediment concentration and erosive event (Miall, 1978, 1996) |
| St Trough cross-stratified sandstone | Reddish and brownish, sub-rounded grains, well- to moderately-sorted, fine-to medium-grained arkosic sandstones, with thin mudstone layer drape on the foresets, regular thick-thin (0.1–0.5 cm) alternations in lamina thickeness. Foresets dipping at low angles (5–10°) | Trough cross-stratification | No fossils | No trace fossils | 0.2–0.4 | Dm-thick wedge-shaped beds. Reactivation surfaces delimiting the foresets. | Migration of subaqueous dunes (3D) by unidirectional flow in lower flow regime. Compound dune/tidal dune of channel infill. Variable energy flow ( Miall, 1978, 1996) |
| Sp Planar cross-stratified sandstone | Sub-rounded grains, well- to moderate-sorted, medium-grained arkosic sandstones, organized in dm-thick | Planar cross-stratification | No fossils | No trace fossils | 0.8 | Tabular beds, typically flat on the top and concave-up base | Migration of 2D subaqueous dunes by unidirectional flow in lower flow regime (Miall, 1978, 1996) |
| Sr Climbing ripple cross-laminated sandstone | Rounded grains, well-sorted, very fine- to fine grained arkosic sandstones | Climbing ripple cross-lamination | No fossils | No trace fossils | 0.25–0.4 | Organized in cm-thick wedge-shaped beds, with flat base | Migration of supercritical climbing ripples by a lower regime unidirectional flow (Miall, 1978, 1996) |
| Smb Massive sandstone bioturbated | Reddish to brownish, sub-rounded to sub-angular grains, well- to moderate sorted, fine- to medium-grained arkosic sandstone, moderate to highly bioturbated | Massive | No fossils | Vertical and horizontal burrows | 0.3–1.0 | Tabular beds with flattered top and base. Obliteration of the primary sedimentary structure | Post-depositional modification by bioturbation (Miall, 1978, 1996) |
| H Heterolithic facies | Grey to beige, well-sorted, sub-rounded grains, very fine- to fine-grained arkosic sandstones with scattered flaser-bedding (mud drapes ~ 0.1 cm) interbedded with linsen and wavy-bedding (10–20 cm) mudstone layers. Mm- to dm-scale interlamination of thin mud-rich and sand-rich layers, arranged in dm- to m-thick beds | Linsen, wavy and flaser beddings | No fossils | No trace fossils | up to 1 | Beds with tabular geometry, normally flattered top and base | They are deposits of shallow bodies of water, under variations in sediment supply and tidal velocity/energy flow (Dalrymple et al., 2003; Dalrymple and Choi, 2007) |
| Hb Herringbone cross-stratified sandstone | Well- to moderate-sorted, sub-rounded to rounded grains, medium-grained arkosic sandstones | Herringbone cross-stratification | No fossils | No trace fossils | 0.3–0.4 | Organized in dm-thick wedge-shaped beds. Reactivation surface in association with bidirectional flow evidence | Deposition under opposite-direction currents, dominated either by flood or ebb currents (Dalrymple and Choi, 2007) |
| F Fines | Red to purple mudstones and siltstones, moderately to highly bioturbated | Massive | Echimonocolpites protofranciscoi, Ulmoideipites krempii, Cricotriporites aff. Macroporus, Proxapertites psilatus, Momipites africanus; Araucariacites sp | Vertical and horizontal burrows | up to 5 | Tabular beds | Decantation in subaqueous environment with very low or absent energy (Miall, 1978, 1996) |
| P Paleosol | Silty shales with mottled aspect; carbonate nodules (2–3 cm); root traces | Massive/ incipient lamination | No fossils | Root traces (undefined) | 5 to 10 | Tabular beds | Long periods of plants colonization, non-deposition or highly probable low rate of accumulation. Process of evaporation conducting to íons concentration and formation of carbonate nodules (Miall, 2006; Nichols, 2009) |
| **Carbonate facies** | | | | | | | |

(*continued on next page*)

Table 1 (*continued*)

| Facies/ Microfacies | Lithology and Texture | Sedimentary Structures | Paleontological content | Ichnology | Thickness (m) | Other characteristics/ Geometries | Interpretation |
|---|---|---|---|---|---|---|---|
| Mp Peloidal Mudstone | Dark brown, fine-grained carbonatic mud matrix (micrite), with scattered peloids grains and minor fine siliciclastic grains | Massive | Peloids | No trace fossils | 0.1–0.2 | Tabular beds with flattered top and base. Peloids (20–200 μm in diameter) are spherical, ellipsoidal and irregular carbonate grains, with no internal structure, moderately-sorted | Organically induced precipitation (Flügel, 2010; Tucker and Wright, 1990) |
| Wpo Wackestone with peloids and ostracods | Dark-brown limestones, mud-supported carbonate rock, composed by ostracods and peloids grains (20–45%). Peloids have clotted textures and the ostracods are normally scattered but are occasionally found oriented parallel to stratigraphic bedding by disarticulated valves | Massive/ incipient lamination | Peloids and Ostracods (200–400 μm) | No trace fossils | 0.2–0.4 | Tabular bed with flattered top and base. Locally, peloids have dense packaging | Deposited under low-energy condition with some water agitations, indicating some transportation (disarticulated valves) (Flügel, 2010; Tucker and Wright, 1990) |
| Woc Wackestone with ostracods and charophytes | Mainly composed by micrite with scattered bioclasts (>10% grains) such as ostracods and charophyte gyrogonites | Massive | Peloids; ostracods (200 μm); charophyte gyrogonites (600–800 μm) | No trace fossils | 0.2–0.5 | Tabular beds with flat base and undulated top. Moldic porosity characterized by molds of ostracods and charophyte remains (both broken and intact) | Deposited under low- to medium-energy condition with some water agitations, indicating some transportation (disarticulated valves) (Flügel, 2010; Tucker and Wright, 1990) |
| Gps Pisolithic Grainstone | Grainstone fabric with dominant occurrence of pisoids. The matrix contain abundant angular to subrounded, moderate to poorly sorted terrigenous quartz grains. Sutured contacts (microstylolitic) and concave-convex contacts (pisoids - quartz grains) | Massive | Pisoids (>2 mm) | No trace fossils | 0.1–0.2 | Brown to red pisoids with dense or irregular laminations, sub-spherical to irregular, partially replaced by pyrite (?) | Biogenic processes or chemical precipitation. Sutured grains related to compaction and pressure dissolution (Flügel, 2010; Tucker and Wright, 1990) |

## 4. Results

### *4.1. Sedimentary facies*

The Juanjuí stratigraphic section is approximately 450 m thick and comprises nine siliciclastic facies and four carbonate microfacies, which are summarized in Table 1.

### *4.2. Facies associations*

#### *4.2.1. Facies association 1 (FA1)*

*4.2.1.1. Description.* Facies association 1 is made up of six facies: Gcm, St, Sp, Smb, Sr and F (Table 1, Fig. 4). Its vertical succession generally displays a fining- and thinning upward, and it typically has a m-scale thickness (5 m). It starts with the channelized bodies of the coarse-grained facies (Gcm) (Fig. 5A and B), which grade to fine-to medium-grained arkosic sandstones with trough (St) (Fig. 5C) and planar (Sp) cross-stratifications, and it ends with cm-scale-thick, very-fine- to fine, climbing-rippled sandstones (Sr) (Fig. 5D) interbedded with the fines facies (F), which is marked by root traces. The channel bodies show discontinuous and cuneiform beds, and they laterally change into interbedded fine-to medium-grained arkosic sandstones. Locally, the fine-grained trough cross-bedded sandstones are arranged in wedge- shaped sets with mm-scale mudstone layers draped over the foresets (St facies) (Fig. 5F), which are highlighted by reactivation surfaces. There are also dm-scale, very-fine-grained deposits with highly bioturbated sandstone (Smb) (Fig. 5E) interbedded with the fines facies (F). FA1 is observed in the lower parts of the Juanjuí section (0–30 m) (Fig. 4).

*4.2.1.2. Interpretation.* Channel body geometries, such as those observed in FA1, are common deposits in tidal and fluvial settings. In both systems, channels reveal an erosive base that internally comprises upward-fining and thinning-up strata that grade upwards into shales and siltstone beds. These fines beds at the top of the succession can characterize either tidal flat or fluvial floodplain deposits (Dalrymple and Choi, 2007).

The massive conglomerates (Gcm) or cross-bedded sandstones (St) with mud clasts at erosive basal surfaces can correspond to fluvial channel filling with reworking lag deposits (Miall, 1996). However, the mud clasts in the bottom channel deposits are also common in tide-influenced environments and can occur due to the erosion of thin, muddy tidal-flat deposits made by high-energy currents (Dalrymple and Choi, 2007). Additionally, the occurrence of thin mudstone layers on the foresets of cross-bedded sandstones (St) associated with reactivation surfaces could be used to infer variations in the current speed and may indicate tidal-flow reversals (Dalrymple and Choi, 2007; Mowbray and Visser,

1984); they suggest deposition in a tide-influenced environment. In conclusion, we interpret facies association 1 as channel deposits formed in the inner part (landward) of a fluvial-tidal transition zone during the early-stage of tide-influenced channel settlement.

*4.2.2. Facies association 2 (FA2)*

*4.2.2.1. Description.* Facies association 2 is composed of five facies: Mp, Wpo, Woc, Gps and F (Table 1, Fig. 4). Laterally, the facies association is represented by dm-to m-scale carbonate tabular beds (Fig. 7A), which commonly occur with a flatten top and base, interbedded with m-scale, red to purple, fine-grained facies (F) (Fig. 6A). It is characterized by cm- to-dm-thick beds of shelly carbonates composed of dispersed to dense microfossils (mainly ostracods and charophytes) and occasionally contains peloids and pisoids. Some beds are hybrid limestone composed of quartz grains and carbonate bioclasts (pisoids) (Gps). The vertical succession shows a coarsening-upward trend that starts with peloidal mudstones (Mp) (Fig. 7B), which grade to the wackestones facies (Wpo; Woc) (Fig. 7C–F) and then to the grainstone facies (Gps) (Fig. 7G); generally, they are interbedded with mm-to-cm thick fine-grained structureless facies (F) (Fig. 4). Poorly developed desiccation-crack surfaces are commonly present at the top of the carbonates and fine- grained beds. The fine-grained facies presented in this facies association contains numerous palynomorphs including *Echimonocolpites protofranciscoi, Ulmoideipites krempii, Cricotriporites* aff. *Macroporus, Proxapertites psilatus, Momipites africanus* and *Araucariacites* sp. (Fig. 6D–G) (Table 1). A microfacies analysis of thin sections made it possible to recognize the micritic matrix, which is mainly attributed to the mudstone facies (Mp) (Fig. 7B), as well as the moldic porosity, which generally indicated molds of ostracod and charophyte remains (Fig. 7F). FA2 has been observed approximately in two intervals of the Juanjuí stratigraphic section: 50–80 m and 292–335 m (Fig. 4).

*4.2.2.2. Interpretation.* FA2 indicates minimum water agitation; sediments were deposited in lower-energy conditions (Flügel, 2010; Tucker and Wright, 1990), with some episodic water agitation attributed to the presence of fragmented ostracods (disarticulated valves) and sporadic terrigenous inflow due to an association with detrital quartz grains, suggesting low sedimentary transport or reworking. The peloid features may be organically induced precipitated features (Flügel, 2010). The charophyte-bearing carbonates are commonly attributed to freshwater environments, as they are ubiquitous in many ancient lake deposits (Tucker and Wright, 1990; Burne et al., 1980). The sedimentary succession presented above is indicative of deposition in a shallow lacustrine environment with evaporation and decantation processes, episodic sediment supply events and subaerial exposition.

*4.2.3. Facies association 3 (FA3)*

*4.2.3.1. Description.* Facies association 3 consists of four facies: P, Smb, Sr and Woc (Table 1, Fig. 4). It is mainly composed of paleosols (P) horizons (Fig. 6C) with scattered gypsum nodules in a very fine matrix, with less-common climbing-rippled sandstone beds (Sr), bioturbated sandstone deposits (Smb) and wackestone with ostracods and charophytes (Woc). The vertical and lateral relations of the facies reveal no significant changes; there are thick paleosol intervals with sparse dm-to- m thick carbonates and sandstones beds.

*4.2.3.2. Interpretation.* The carbonate nodules occurring in the paleosol intervals represent ions concentrations during processes of evaporation and capillary groundwater flow in arid periods (Nichols, 2009; Miall, 2006), indicating seasonal water fluctuations. Paleosols with root traces can indicate long periods of non-deposition and plant colonization or a low rate of accumulation.

*4.2.4. Facies association 4 (FA4)*

*4.2.4.1. Description.* Facies association 4 is composed of seven sedimentary facies: Smb, St, Sp, Sr, Hb, H and F (Table 1, Fig. 4). The vertical facies association displays a coarsening and thickening upward into the section, which grades from very-fine- to medium-grained sandstones and cm-to-dm-thick to dm-to-m-thick beds. The section generally varies laterally; it is characterized by the dm-thick heterolithic facies (H) (Fig. 5G) interbedded with fines (F) and fine-to medium grained cross- bedded (St) and climbing-rippled (Sr) sandstones. Occasionally, it shows herringbone cross-stratification (Hb) (Fig. 5H) or planar cross- bedded (Sp) sandstones. The medium-grained cross-bedded (St) sandstones can present dm-thick wedge-shaped beds, with a concave-up base and mm-scale mudstone layers draped over the foresets (St facies), which are highlighted by reactivation surfaces, grading to climbing- rippled (Sr) sandstones. The highly bioturbated sandstones (Smb) are commonly interbedded with the fines (F) facies, showing no lateral variation. FA4 was recognized in the upper part of the present section, in the interval from about 380 to 442m.

*4.2.4.2. Interpretation.* Heterolithic facies with flaser, wavy and linsen bedding, cross-bedded sandstones with thin mudstone drapes on the foresets, reactivation surfaces and herringbone cross-bedded sandstones point to an environment influenced by tidal currents. The presence of reactivation surfaces might have been caused by tidal current reversals (Thomas et al., 1987; Mowbray and Visser, 1984; Klein, 1970) although these surfaces could also be produced by river-discharge variations in fluvial settings (Dalrymple, 1984). Despite the fact that the H facies can be observed in river-dominated settings (Johnson and Dashtgard, 2014), the mud-sand-mud profile is not observed in bars further landward (Dashtgard and

Gingras, 2012) and is more common in tide-dominated systems (Dalrymple and Choi, 2007; Dalrymple and Choi, 2003). Reactivation surfaces and mud layers might occur in fluvial point bar deposits (Collinson, 1996; Miall, 1996).

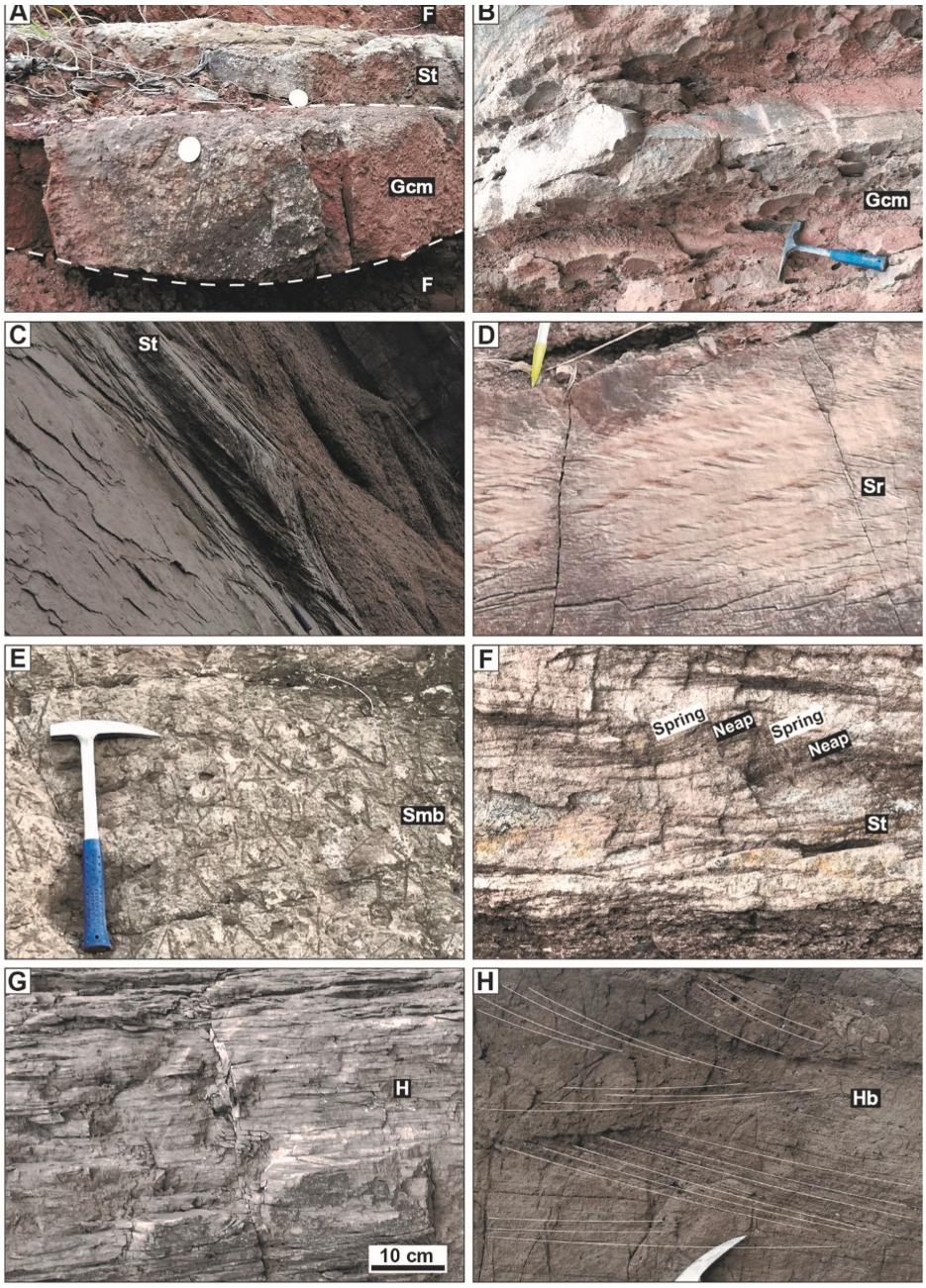


**Fig. 5.** Representative photographs of the siliciclastic facies. A) Massive clast-supported conglomerate (Gcm) with an erosive base, limited between fines with no structures (Fm) (below) and sandstones with through cross-stratification (St) (above); B) Massive conglomerates with scattered clasts (Gcm); C) Fine-grained sandstone with through cross-stratification; D) Fine-grained sandstone with climbing ripples; E) Highly bioturbated deposits (Smb) covering the primary structures in fines bodies; F) Thin mudstone layer drape on foresets of cross-bedded (St) fine-grained sandstones with regular variations (neap-spring influence); G) Heterolithic facies (H) with flaser bedding; H) Fine to medium-grained sandstones with bi-directional herringbone cross-stratification (Hb).

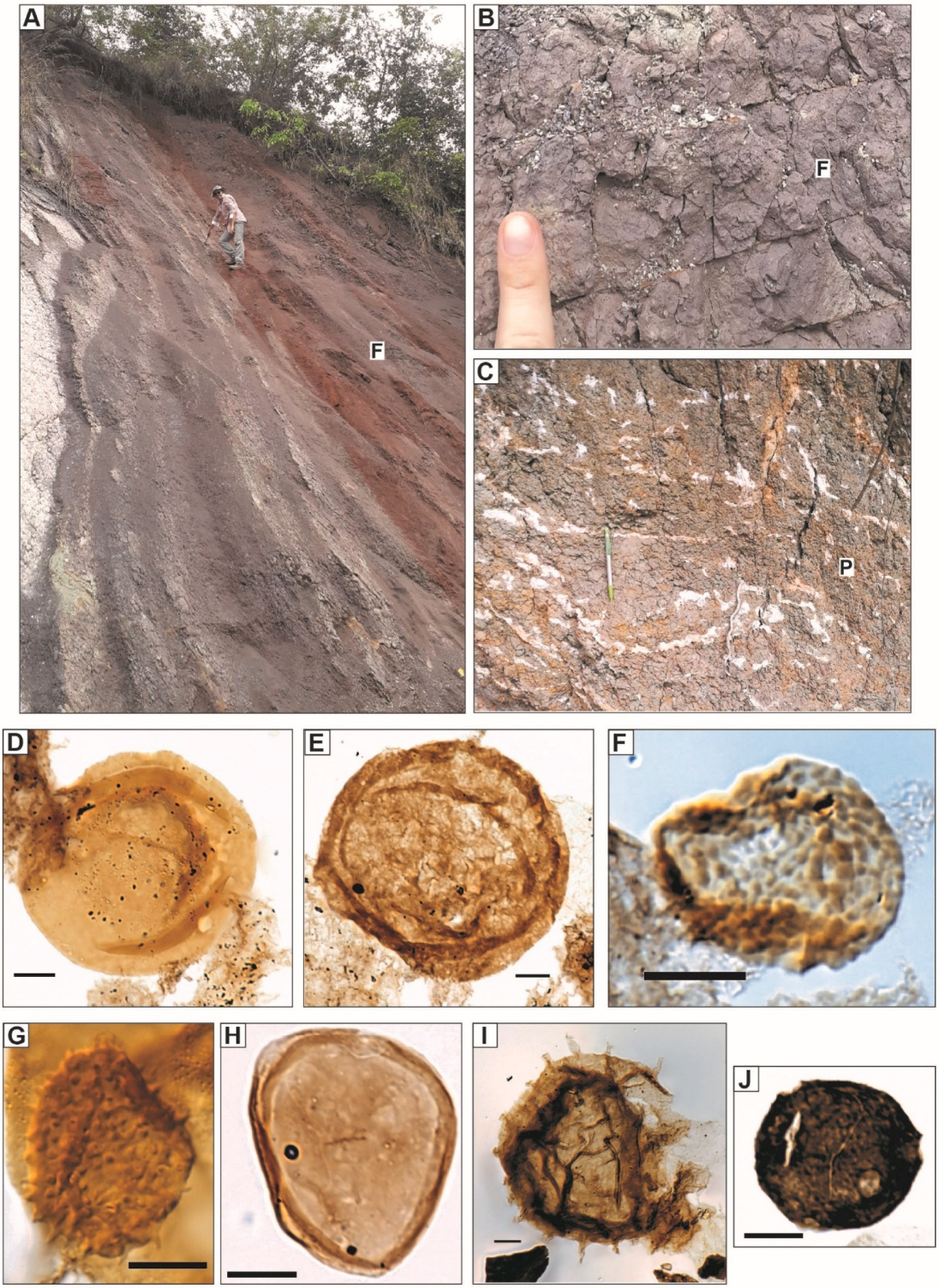


**Fig. 6.** Fine-grained facies; paleosols and palynological content. (A) Overall m-scale view of massive mudstones and siltstones, with red to purple colors, interbedded with cm-dm tabular carbonate beds. (B) Massive siltstones, presenting purple to green-grey colors, latter probably related to weathering processes. (C) Paleosols with incipient horizontal lamination, mottled horizons. (D) *Cricotriporites* aff. *Macroporus*, slide 47,176_A, England Finder (EF) W13; (E) *Araucariacites* sp., slide 47,176_A, EF N12/2; (F) *Ulmoideipites krempii*, slide 47,176_A, EF S8/4; (G) *Echimonocolpites protofranciscoi*, slide 47,176_A, EF Q12/1; (H) *Proxapertites psilatus*, slide 47,179_B, EF F15; (I) *Balmeisporites minutus*, slide 47,179_B, EF S33/4; (J) *Momipites africanus*, slide 47,179_B, EF M5/2. Scale bars = 10 µm.

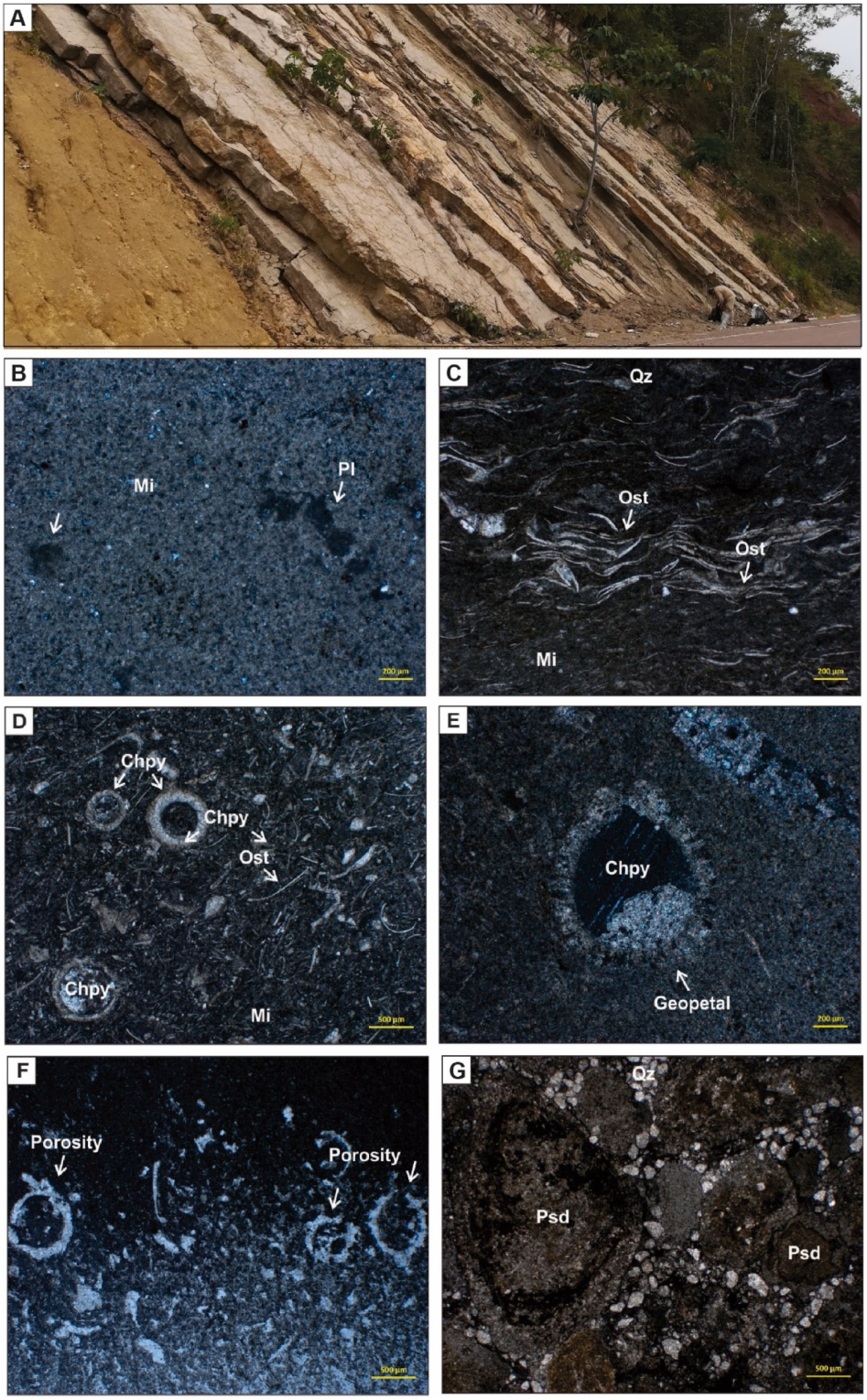


Fig. 7. Representative photographs of carbonate microfacies. A) General view of the carbonate outcrops; B) Mudstone deposits with scattered peloids (Mp) with clotted texture (HUA63B); C) Dark-brown wackestones with peloids and ostracods (Wpo) (HUA63C), characterized by disarticulated valves of ostracods oriented parallel to bedding of rock; D) Wackestone with scattered bioclasts as fragmented ostracods and charophytes (Woc) (JUA5A); E) Geopetal structure and recrystallized by spar marked in the inner part of charophytes (JUA5B); F) Moldic porosity is identified as secondary pores in charophytes (JUA5C); G) Fragments of pisoids partially replaced by pyrite (?) (JUA 2 B). Mi = micrite; Pl = peloids; Ost = ostracod; Chpy = charophyte; Psd = pisoid.

The occurrence of bidirectional trough cross-bedding (Fig. 5H) suggests a depositional area that received opposite-direction currents, which are characteristic of a tide-dominated environment (Longhitano et al., 2012) and can be either flood or ebb currents. The regular variations in the lamina thickness characterize rhythmic sedimentary structures, which are well documented in subtidal channels (Allen and Homewood, 1984; Visser, 1980), and they could be interpreted as the influence of a neap-spring tidal cycle (Flemming, 2012; Dalrymple and Choi, 2007). In conclusion, we interpret facies association 4 as deposits formed in the distal part of a fluvial-tidal transition zone.

### *4.3. Depositional environments*

The integration of the sedimentary facies association, paleontological content and stable isotopic compositions make it possible to characterize two depositional systems during the Maastrichtian-Bartonian: a tide-dominated depositional system and a lacustrine deposition system (Figs. 4 and 10).

#### *4.3.1. Tide-dominated environment: the fluvial-tidal transition zone*

The tide-dominated depositional system was recognized in the Maastrichtian and late middle Bartonian (Figs. 4 and 10A, C). This depositional system is composed of two facies associations: FA1 and FA4.

During the Maastrichtian (0–40 m along the section), FA1 generally prevails, and it is mainly composed of m-scale coarse-grained channelized shapes with upward-fining and thinning-up strata. The vertical stacking pattern and lateral changes of conglomerate facies to sandstone and finer facies were most probably related to a proximal area within a fluvial-tidal transition zone (landward) that experienced a less-tide-dominated influence. These Maastrichtian tidal deposits can be correlated with those of the Vivian-Cachiyacu-Huchpayacu formations (Calvès et al., 2018; Hurtado et al., 2018; Louterbach et al., 2014).

During the late-middle Bartonian (~350–450 m), FA4 is more abundant than FA1. The sedimentary stacking pattern reveals a tide-dominated environment, which is mainly represented by heterolithic facies interbedded with fines and climbing-rippled beds and also by typical tidal-current reversal deposits, such as herringbone cross-bedded sandstones. Reactivation surfaces and herringbone cross-bedding are more common in the distal area within a fluvial-tidal transition zone (seaward direction), where it is possible to recognize tidal bundles (Dalrymple and Choi, 2007). Compared with the Maastrichtian sedimentary rocks, these deposits are more deeply bioturbated. These Bartonian tide-influenced deposits can be correlated with the shallow marine deposits of the Pozo Fm. (see Roddaz et al., 2010, and the references therein).

*4.3.2. Lacustrine environment*

The lacustrine depositional system was recognized in the Maastrichtian and the Lutetian (Figs. 4 and 10A, B). This depositional system is composed of two facies associations: FA2 and FA3.

The lacustrine setting starts with FA2. The sedimentary stacking pattern is mainly composed of continuous carbonate beds interbedded with shales and siltstone beds with a coarsening-upward trend; Gps and Woc are present at the top of the succession (Fig. 4). This facies association occurs from approximately 50 to 80 m and from 292 to 350 m. This facies association was deposited under absent to low-energy hydrodynamic conditions, recording a shallowing-upward succession. The carbonates at the base of the sequence are mainly composed of the mudstone peloidal facies (Mp), which grades to the wackestones (Wpo, Woc) and grainstones (Gps) facies at the top. The sedimentary features observed in FA3 indicate a transition from ephemeral events under arid conditions to a period of low accumulation rates or long periods of non- deposition. The dominance of mudstone facies and the poor development of grainstone facies are interpreted to reflect lower wave energies and point to shallow lake environments (Platt and Wright, 1991). This agrees with the presence of charophytes, which are the dominant carbonate producers in low-energy and shallow freshwater settings (Platt and Wright, 1991). The lacustrine carbonates/shelly strata represented by FA2 and FA3 can be correlated with the fluvial-lacustrine Yahuarango Fm. (Roddaz et al., 2010; Hermoza et al., 2005; Gutiérrez, 1982; Kummel, 1948).

*4.4. Oxygen and carbon stable isotopes*

The results and variations of the stable isotopic compositions (C, O) of the analyzed samples are presented in Figs. 4 and 9, and Table S2 (Supplementary Material). The analyzed stable isotopic data were compared with stable isotope values from Amazonian Miocene fossils (Alvim et al., 2021). North American rivers, the Great Lakes, North Atlantic seawater, the Black Sea and the San Francisco Bay estuary (Varol, 2015; Logvina et al., 2004; Ingram et al., 1996; Keith et al., 1964) (Fig. 9). It is important to emphasize that, despite using the stable iso- topic compositions of modern sites distinct from our localities, the isotopic fractionation processes at these sites are likely to have occurred in similar environments (e.g., lakes, estuaries or seas).

The succession exhibits significant variations in $\delta^{13}C$ and $\delta^{18}O$, as shown in Fig. 3. In the first 53 m from the base to the top, the $\delta^{13}C$ values increase from –11.5 to –4.2‰ (JUA 1 A-E) (Fig. 4, Table S2). Between 53 and 82 m, most samples range from –7.3 to –6.0‰, except for the sample JUA 2 B, which presents a strong negative carbon isotopic value (–11.1‰). Between 82 and 350 m (Lutetian), the $\delta^{13}C$ values increase slightly to between

–10.0 and –2.8‰, and then they shift to low values (–11.9 to –10.0‰) in the upper part of the series (Bartonian).

The $\delta^{13}C$ and $\delta^{18}O$ values for the analyzed samples are negative, varying between –11.9 and –2.8‰ and from –10.2 to –1.1‰, respectively (Figs. 4 and 9). The youngest samples (located between 382 and 392 m in Fig. 4) are characterized by the most negative $\delta^{13}C$ values and plot within the North America river isotopic field. The isotopic compositions of the Lutetian samples are more scattered. Most of the samples have isotopic compositions similar to those of the Contamana Neogene fossils analyzed by Alvim et al. (2021) (dinoflagellate-, oyster- and foraminifer-yielding beds CTA-77 and CTA-58). Four samples are characterized by negative $\delta^{18}O$ values and plot between the Great Lakes and NA river fields (Fig. 9). The four youngest samples that are associated with the TAR-78 fossil-bearing site have the highest $\delta^{18}O$ values and plot close to or within the isotopic field of the San Francisco Bay (Fig. 9). The Lutetian samples plot mostly between the NA river and Great Lakes fields, whereas the Maastrichtian and Bartonian samples have $\delta^{13}C$ and $\delta^{18}O$ values within or close to the NA river field (Fig. 9).

Carbon and oxygen isotopic data exhibit isotopic values that indicate non-marine environmental conditions ($\delta^{13}C$ from –11.9 to –2.8‰ VPDB and $\delta^{18}O$ from –10.2 to –1.1‰ VPDB (Figs. 4 and 9). According to the isotopic signatures, the deposits present a covariance of negative $\delta^{13}C$ and $\delta^{18}O$ isotopic compositions, which could support predominantly freshwater conditions (Vonhof et al., 1998). The $\delta^{13}C$ and $\delta^{18}O$ isotopic values of the upper part of this depositional system (samples HUA 473 N to Q, located from ~311 to 333 m; Fig. 4) are much less negative ($\delta^{13}C$ ranging from –8.2 to –2.8‰ and $\delta^{18}O$ from –6.6 to –1.1‰) (Figs. 4 and 9 and S2), which could reflect a transition to brackish conditions in an estuarine depositional system (Figs. 4 and 9) (Ingram et al., 1996). The fossil record is also in agreement with this paleoenvironmental transition, from freshwater to brackish conditions, which is indicated by the presence of i) marine, estuarine or brackish pycnodontiform ray-finned fish and myliobatiform selachians (*Potobatis* and *Ouledia*; Fig. 8D) at TAR-30, and ii) pelomedusoid turtles, of brackish affinities at TAR-78.

*4.5. Biostratigraphic constraints: paleontological content of the Juanjuí Maastrichtian–Eocene section*

The TAR-59 sample (labeled in green in Fig. 4) provided no macro- fossil content, but crushed bone fragments, most likely documenting medium-sized dinosaurs, were retrieved from JUA 1 B, 30 m below in the same section (Fig. 4). Conversely, a palynological sample (TAR-PN-16-09) yielded an assemblage dominated by the freshwater algae *Pediastrum* (about 98% out of 300 grains counted) and other panchronic taxa, such as the fern spore *Laevigatosporites* sp.,

dinocysts assignable to *Batiacasphaera*, and reworked acritarchs.

The TAR-29 sample (labeled in green in Fig. 4) has yielded charophyte oogonia by the thousands (unidentified), silicified plant cuticles, unidentified turriform gastropods, ostracods (under study), freshwater bony fish remains (pacu-like characiform teeth and loricariid siluriform iridescent dermal scutes), chelonian osteoderm fragments, a paddling-turtle trackway (collapsed in 2015; Fig. 8A) and waterbirds regurgitated pellets (with numerous fish scales and spines; Fig. 8B) in the uppermost levels of the exposure. Unfortunately, this assembly does not allow any precise biostratigraphic dating. Conversely, palynological samples TAR-29-PN2/19 (stratigraphic meter 79), TAR-29-PN4A-19 (stratigraphic meter 81.4) and TAR-29-PN5-19 (stratigraphic meter 81.6) from the same sample point to a Maastrichtian age (based on the palynological zonation of Jaramillo et al. (2011) and De La Parra et al. (2021)). They are characterized by rich terrestrial organic matter and palynomorphs (Fig. 6D–J), including abundant *Araucariacites* (gymnosperm), *Gnetaceaopollenites* (gymnosperm), *Pediastrum* (freshwater algae), *Echimonocolpites protofranciscoi* (angiosperm), *Ulmoideipites krempii* (angiosperm), *Longapertites* (angiosperm, palms), *Cricotriporites* aff. *Macroporus* (angiosperm), *Echitriletes selaginelloides* (fern), *Racemonocolpites* (angiosperm, palm), abundant *Proxapertites psilatus* (gymnosperm Araceae), *Momipites africanus* (angiosperm), *Foveotriletes* aff. *Margaritae* (fern) and *Balmeisporites minutus* (fern). The additional palynological samples TAR-29-PN1/19, TAR-29-PN3/19 and TAR-29-PN4/19 did not provide useful results.

Aside from unidentified charophyte oogonia and ostracods (under study), the TAR-30 sample (base top) yielded a species-rich fish assemblage, with ray-finned taxa (characins: pacu- and piranha-like teeth; iridescent dermal scutes of loricariid siluriforms; *Stephanodus* pharyngeal teeth; Fig. 8E), selachians (Myliobatiformes: the batoid *Ouledia* sp. (Fig. 8D) and the dasyatoid *Potobatis*) and dipnoans (Ceratodontidae/Lepidosirenidae). *Ouledia* (Thanetian–Priabonian) and *Potobatis* (Danian–Thanetian) had also been recognized in shallow marine-influenced Thanetian deposits of the Madre de Dios Basin, in association with pycnodontiform pycnodontids (Louterbach et al., 2014). The TAR-30 fauna also includes turriform gastropods, pelomedusoid turtle shell fragments, and crocodylomorph teeth. As a whole, the fauna point to a Thanetian biostratigraphic age, which is supported by close affinities with the Thanetian ichthyofauna of the Madre de Dios Basin (Louterbach et al., 2014), at least in the absence of younger strata yielding similar assemblages.

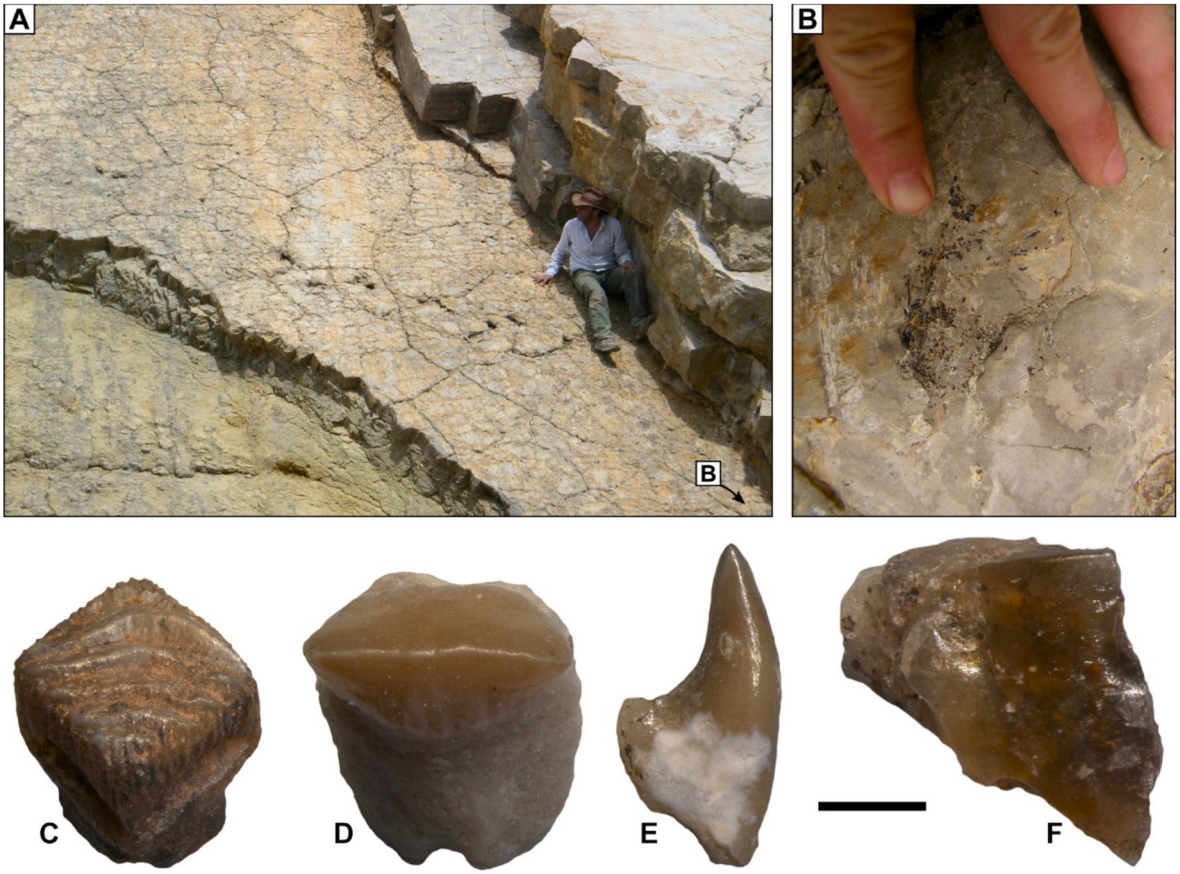


**Fig. 8.** Selected vertebrate-related findings and vertebrate fossils of interest from the Maastrichtian–Paleogene Juanjuí section, San Martín, Peru. A) Paddling-turtle track at TAR-29 (=HUA-63; Maastrichtian). The turtle was moving to the right. The same carbonated layer provided the regurgitation ball seen in B; B) Regurgitation ball (of an aquatic bird?), with fish bones and scales both gathered and split all around (TAR-29 = HUA-63; Maastrichtian); C) *Pucapristis hoffstetteri*, tooth in occlusal view (TAR-41, Maastrichtian); D) *Ouledia* sp., tooth in occlusal view (TAR-30 sup. = HUA-473; Lutetian); E) *Stephanodus* sp., pharyngeal tooth in lateral view (TAR-30 sup. = HUA-473; Lutetian); F) Polypterid polypteriform, fragmentary ganoin scale in external view (TAR-42 = JUA 14; Bartonian). Scale bar = 1 mm (C, E) and 0.5 mm (D, F).

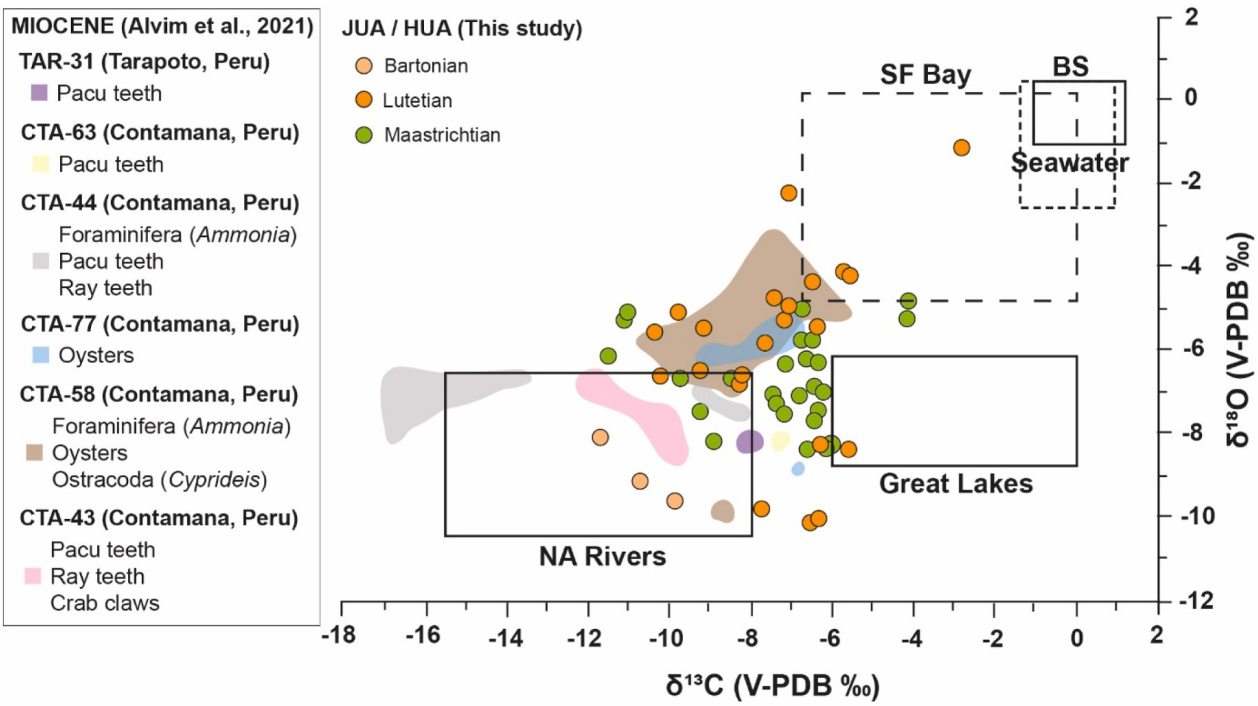


**Fig. 9.** Carbon versus oxygen isotopes cross plot of Miocene (Alvim et al., 2021) and Eocene fossil and carbonates samples. Black boxes represent stable isotopes values of modern mollusks from North Atlantic seawater, Great Lakes, and North American rivers (Keith et al., 1964), the San Francisco Bay estuary (Ingram et al., 1996) and the Black Sea (Varol, 2015).

The TAR-78 sample yielded charophyte oogonia and half a carapace of a pelomedusoid turtle, of brackish affinities (under study by Edwin Cadena).

At the top of the studied section, the TAR-42 sample yielded a ganoin scale of a polypterid polypteriform (*Latinopollia* or *Dagetella*; Fig. 8F), as well as turtle shell fragments, a large crocodylomorph osteoderm, and a fragmentary lower molar of a tiny South American native ungulate (SANU), documenting a panperissodactyl (Notoungulata or Litopterna). The last appearance datum (LAD) of polypteriforms in South America is Paleocene in age (Gayet et al., 2002). The occlusal pattern and dimensions of the panperissodactyl are in good agreement with a Thane- tian–Ypresian biostratigraphic age and at odds with post-early Eocene SANUs.

*4.6. U–Pb ages*

Table 2 present the U–Pb zircon ages for the analyzed Cenozoic sedimentary rocks. Details on individual U–Pb zircon ages for each sample can be found in the supplementary material (Tables S2–S6).

The zircon population of the Cenozoic samples is dominated by grains from the Eocene Andean Arc (<0.065 Ga) (Table 2). The other dominant zircon populations are Grenville Sunsás (1.3–0.9 Ga) and to a lesser extent, Rondonia-San Ignacio (1.54–1.3 Ga) and Rio Negro-Jurena (1.82–1.54 Ga).

The maximum depositional ages (MDAs), calculated as the weighted mean of YC2σ[+3] following Sharman and Malkowski (2020), are Eocene MDAs. The MDAs decrease up-section from ~43.1 ± 0.29 Ma (Lutetian, JUA 8A/19), to ~42.6 ± 0.32 Ma (Lutetian, JUA 11) and ~38.6 ± 0.19 Ma (Bartonian, JUA 14) in the upper part of the section (Fig. 4, Table S2). The calculated maximum likelihood ages (MLAs) following Vermeesch (2021) are also Eocene ages. The MLAs range from ~43.5 ± 0.64 Ma (Lutetian, JUA 8A/19) to ~42.68 ± 0.66 Ma (Lute tian, JUA 11) and ~37.64 ± 0.85 Ma (Bartonian - Priabonian, JUA 14) (Fig. 4, Table S2). Overall, the MDAs and MLAs are quite similar, and they both decrease up-section.

**Table 2**
Table showing the number and percentage U–Pb ages of zircons grains by distinct geochronological events in potential source areas on the Amazon craton and the northern central Andes. Temporal ranges of events according to Bahlburg et al. (2009), Chew et al. (2008) and Reimann et al. (2010). (n) is the number of samples analyzed for the time interval.

| Time (Ga) | Province/Event | EOCENE | Lutetian | | Bartonian |
|---|---|---|---|---|---|
| | | | JUA 8A-19 | JUA 11 | JUA 14 |
| | | | n = 69/77 | n = 102/120 | n = 102/112 |
| | | | (%) | (%) | (%) |
| <0.065 | Cenozoic Andean Arc | | 14 | 28 | 38 |
| 0.145–0.065 | Cretaceous Andean Arc | | 4 | 0 | 2 |
| 0.25–0.145 | Triassic-Jurassic | | 0 | 1 | 7 |
| 0.4–0.26 | Paleozoic Magmatic Arc | | 6 | 3 | 3 |
| 0.5–0.4 | Famatinian | | 3 | 4 | 2 |
| 0.7–0.5 | Brazilian | | 12 | 13 | 6 |
| 0.9–0.7 | | | 6 | 1 | 2 |
| 1.3–0.9 | Greenville Sunsás | | 29 | 33 | 25 |
| 1.54–1.3 | Rondonia - San Ignacio | | 3 | 7 | 8 |
| 1.82–1.54 | Rio Negro - Jurena | | 10 | 6 | 7 |
| 2.0–1.82 | Ventuari - Tapajós | | 6 | 1 | 0 |
| 2.2–2.0 | Maroni - Itacaiunas | | 6 | 2 | 0 |
| >2.2 | Central Amazon | | 1 | 1 | 0 |

## 5. Discussion

### *5.1. Age of the deposits*

The first stratigraphic constraint regarding the studied sedimentary section is the biostratigraphic age of the TAR-59 sample. This locality yielded unambiguous dinosaur fossil remains. In addition, large dinosaur footprints were identified at the TAR-33 outcrop that can be correlated with the TAR-59 sample (Supplementary Data S7); these footprints are consistent with the Maastrichtian interval (72.1–66.0 Ma) (Fig. 4 and Supplementary Data S7). The TAR-59 sample has the same stratigraphic position as the HUA 63 sample (Fig. 4), which was previously studied by Hurtado et al. (2018). Originally, a Danian age was assigned to HUA 63 (Hurtado et al., 2018) because it was mistakenly supposed to be

intercalated between the TAR-29 fossil site, which yielded a rich charophyte assemblage with a composition similar to the Danian beds of the Ucayali Basin (Agua Caliente, CTA-54 locality; Antoine et al., 2016), and TAR-30, which yielded a rich ichthyofauna, notably including the Danian dasyatid marker *Potobatis* sp. (Cappetta and Gayet, 2013). However, our revised fieldwork suggests that HUA 63 is located below the TAR-29 sample, and is associated with the TAR-59 fossil site instead (Fig. 4). The presence of several key biostratigraphic palynomorphs, including *Echimonocolpites protofranciscoi, Ulmoideipites krempii, Momipites africanus* and *Foveotriletes aff. margaritae*, which were found in the TAR-29 sample (PN2/19, PN4A-19, and PN5-19 located at 79, 81.4 and 81.6 m above the stratum level, respectively) also suggest a Maastrichtian age. Hence, the first 150 m of the Juanjuí sedimentary section as a whole may be ascribed to the Maastrichtian Cachiyacu Fm. Moreover, the contact between Maastrichtian and the overlying Cenozoic sedimentary rocks is located at ~150 m in the sedimentary section (Fig. 4). Paleosol horizons are found above and below this contact (Fig. 4). Paleosol horizons are found above and below this contact (Fig. 4).

Above these paleosol horizons, the three analyzed Cenozoic sedimentary rocks presented MDAs that range from the Lutetian (JUA 8A/ 19, 43.1 ± 0.29 Ma, located at 170 m, and JUA 11, 42.6 ± 0.32 Ma, located at 375 m) to the Bartonian (JUA 14, 38.6 ± 0.19 Ma) located at 440 m (Fig. 4). The MLAs of the analyzed samples show similar Lutetian (JUA 8A/19, 43.5 ± 0.64 Ma), and JUA 11, 42.7 ± 0.66 Ma) and Bartonian to Priabonian ages (JUA 14, 37.6 ± 0.85 Ma) (Table S6). These MDAs and MLAs are significantly younger than the biostratigraphic ages obtained from the fossil-rich outcrops TAR-30, TAR-78 and TAR-42. The JUA 8/19 A samples, which yield a Lutetian MDA (43.1 ± 0.29 Ma), are stratigraphically below the TAR-30 outcrop, which has a Thanetian biostratigraphical cachet, based on the co-occurrence of the selachians *Potobatis* and *Ouledia* (Paleocene and Thanetian–Priabonian ranges, respectively; Louterbach et al., 2014, and the references therein). Similarly, the Bartonian to Priabonian zircon MDAs and MLAs of sample JUA 14 are significantly younger than the Thanetian–Ypresian bio- stratigraphical age of TAR-42 (which yielded polypterid scales of presumed Maastrichtian–Paleocene age and a tiny early-diverging SANU of Paleocene–early Eocene hypothesized affinities), which is situated at the same stratigraphic level. In both cases, this temporal discrepancy may be related to unexpected longer stratigraphical ranges of remarkable fossil taxa, due to last appearances much younger than previously thought for *Potobatis* (world scale) or *Ouledia* and the polypterids (South American scale).

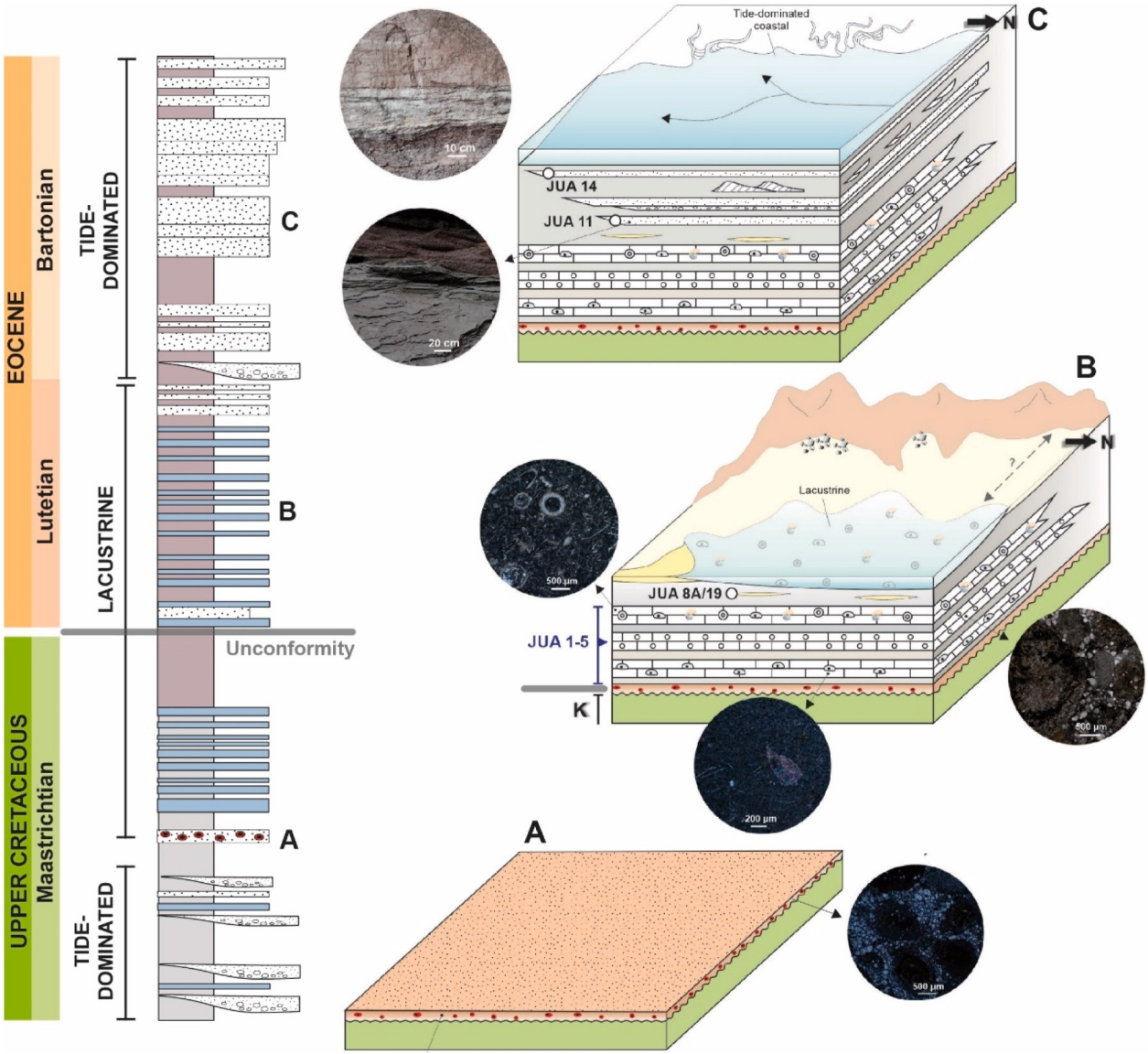


Fig. 10. Schematic composite section and 3D sketch representing the paleoenvironmental reconstruction of the (A) Maastrichtian – Paleogene stratigraphic un- conformity, (B) Lutetian lacustrine setting, (C) The Bartonian transition from lacustrine system to the tide-dominated setting, represented by the distal part in a fluvial-tidal transition zone. See text for details.

According to the MDAs and MLAs, the faunal content of the fossil site TAR-30 may not be Danian but Lutetian in age and the fossil sites TAR-78 and TAR-42 are Lutetian and Bartonian in age, respectively (Fig. 4). These results suggest that i) the analyzed samples are part of the Eocene Pozo Fm. (Roddaz et al., 2010), and ii) contrary to what was published in Roddaz et al. (2010), the Paleocene Yahuarango Fm. may be absent in the Huallaga Basin.

*5.2. Paleogeographic implications*

Our multi-disciplinary dataset provides new constraints on the paleoenvironmental evolution of Western Amazonia during the Maastrichtian – Bartonian (late middle Eocene).

Our data suggest that a tide-dominated system occupied the Huallaga Basin during the Maastrichtian. Previous paleogeographic reconstructions of the late Cretaceous configuration of Peruvian Western Amazonia also suggest that the Madre de Dios and Marañon basins were characterized by shallow marine deposits during the Campanian–Maastrichtian (Louterbach et al., 2018b; Zamora and Gil, 2018). In Ecuador, the Maastrichtian basal Tena sandstones of the Oriente Basin are also interpreted to represent tide-dominated deposits (Jaillard et al., 2005). The Upper Cretaceous units in neighboring basins (e.g., Vivian and Cachiyacu formations in the Santiago, Marañon and Madre de Dios basins) are also characterized by shallow marine paleoenvironments (Zamora and Gil, 2018, and the references therein). A coastal paleo-environment is also suggested in the Bagua Basin (Moreno et al., 2020). As already emphasized by previous published studies (Hurtado et al., 2018; Zamora and Gil, 2018), this suggests that Western Amazonia basins were entirely flooded by an epicontinental sea at some point by the Maastrichtian.

At the Cretaceous–Paleogene boundary, a marine-to-continental transition was recorded in the northernmost part of the Andes, coeval with regional records for the onset of compressional deformation in the northern Andes (Central and Eastern Cordilleras) (Zapata et al., 2021; Bayona et al., 2021; George et al., 2019; Gutiérrez et al., 2019; Odoh et al., 2019; Horton, 2018). This transition from shallow marine/coastal to continental paleoenvironments is also recorded in the Huallaga Basin, but it occurred during the Maastrichtian, as indicated by the transition from a tide-dominated depositional system to a continental lacustrine depositional system.

Our new stratigraphic constraints suggest that the Paleocene-to- lower Eocene interval (66–47.8 Ma) may be documented by a 2-m-thick paleosol facies (Fig. 4), indicating that a stratigraphic unconformity may separate the Maastrichtian from the Lutetian–Bartonian sedimentary sequences of the Huallaga Basin (Figs. 4 and 10). A similar chronostratigraphic hiatus was observed to the north in the Oriente Basin (Ecuador) where the sedimentary deposits of the Lower Eocene Tiyuyacu Fm. unconformably overlie the Upper Cretaceous Tena Fm. (Gutiérrez et al., 2019). In Colombia, a regional unconformity was recognized on the eastern side of the Southern Llanos Basin (Colombia), which separates the pedogenized

Cretaceous rocks from the overlying Middle or Upper Eocene rocks (Caballero et al., 2020). To the northwest, in the Bagua Basin (Peru) (Fig. 11A), the Paleocene series are also absent, as shown by i) the absence of Paleocene MDAs obtained for U–Pb in zircons in the Upper Cretaceous to Miocene sedimentary rocks of the Bagua Basin (Moreno et al., 2020), and ii) the presence of a low-angle unconformity between the Campanian–Maastrichtian Fundo el Triunfo Fm. and the overlying Lower Eocene Rentema Fm. (54.2 ± 6.4 Ma) (Naeser et al., 1991). This regional unconformity could be generated by the presence of a migrating forebulge in response to Andean tectonic loading or tectonic quiescence (Horton, 2022). However, we believe that a forebulge unconformity is unlikely to have generated the Maastrichtian-to-Lutetian unconformity recorded in the Huallaga Basin, since an Andean provenance is recorded below and above this unconformity (HUA 63 in Hurtado et al. (2018) and JUA 8A/19 in this study). Following Horton (2022), we propose that a tectonic quiescence marked by a prolonged pause in crustal shortening and flexural loading may have promoted isostatic rebound and the development of an unconformity. In this scenario, we suggest that the Paleocene corresponded to a stage of tectonic quiescence in the Huallaga Basin.

In the Madre de Dios Basin, previous paleogeographic re- constructions suggest that a shallow marine transgression occurred during the late Paleocene (Louterbach et al., 2014). At the time of the publication of this article, the entrance of this shallow marine transgression (Atlantic Ocean, Pacific Ocean or Caribbean Sea) was still unclear. Here, we suggest a southern connection with the Atlantic Ocean (Bolivia–Argentina) through the Parana Sea (Fig. 11A), given the absence of Paleocene deposits in the Huallaga, Bagua and Llanos basins. In this scenario, the upper Paleocene shallow marine deposits of the Madre de Dios Basin may represent the northern end of the Paleocene Parana Sea, which is also recorded by deeper marine deposits in the southern basins, such as the Potosí and Chaco basins (Cappetta and Gayet, 2013; Sempere et al., 1997).

Our data also recorded a shallow marine transgression that may have started during the Bartonian (Late middle Eocene), as indicated by the presence of a tide-dominated coastal depositional system (FA4) (from 42.6 to 38.6 Ma) that overlies the Lutetian lacustrine system (FA2 and FA3). In a tide-dominated estuarine setting, bidirectional currents are likely to be present in the meandering part of the tide-dominated estuary (Dalrymple and Choi, 2007; Dalrymple et al., 1992). This Bartonian shallow marine incursion could be correlated with the Eocene Pozo shallow marine transgression (Hoorn et al., 2010b; Roddaz et al., 2010) that affected the Marañón Basin, which is located east of the studied area (Roddaz et al., 2010; Hermoza et al., 2005; Hermoza, 2004). Moreover, this shallow marine incursion was also recorded in the Santiago Basin (George et al., 2019), within the Pozo and Capas Rojas formations. Based on i) the absence of Eocene deposits in the southern Peruvian Madre de Dios and northern Bolivian Beni basins (Louterbach et al., 2018a; Louterbach et al., 2014; Roddaz et al., 2010; Hermoza, 2004), the presence of ii) Upper middle Eocene shallow marine sedimentary rocks (from 42 to 37 Ma) in the

Colombian Llanos Basin (De La Parra et al., 2021) and iii) the presence of Eocene shallow marine deposits in the Ecuadorian Oriente Basin (Roddaz et al., 2010; Christophoul et al., 2002), a northern entrance through the Caribbean Sea is suggested for this Bartonian transgression (Fig. 11B).

## 6. Conclusions

The multi-disciplinary study (biostratigraphy, sedimentological data, U–Pb zircon ages, and stable isotope composition) of the Upper Cretaceous–Paleogene sedimentary rocks documented in the Juanjuí stratigraphic section of the Huallaga Basin yields the following conclusions.

- The maximum depositional U–Pb zircon ages of analyzed samples became younger up-section with peak MDAs at 43.1 ± 0.29 Ma, 42.6 ± 0.32 Ma and 38.6 ± 0.19 Ma, and MLAs at 43.5 ± 0.64 Ma, 42.7 ± 0.66 Ma and 37.6 ± 0.85 Ma. These data make it possible to refine the stratigraphic age of the studied section and reveal that the Maastrichtian sedimentary sequence is separated from the Lutetian–Bartonian sequence by a stratigraphic unconformity.
- The Upper Cretaceous-Eocene sedimentary rocks of the Huallaga Basin are characterized by two depositional systems: a tide-dominated system and a lacustrine system.
- Two marine transgressions occurred during the Maastrichtian and Bartonian epochs. They are dominated by brackish to freshwater tide-influenced siliciclastic sequences that indicate the presence of a regional embayment in northwestern South America during these time intervals.
- The middle Eocene interval (Lutetian) is characterized by the establishment of a lacustrine setting with contrasting seasons (wet and dry).

The presence of a shallow marine incursion in Western Amazonia during the Eocene might have involved biogeographical isolation, and as such, it may have promoted allopatric speciation for terrestrial organisms. This biogeographic context may have thus played a role in shaping the emergence of post-Paleogene regional biodiversity.

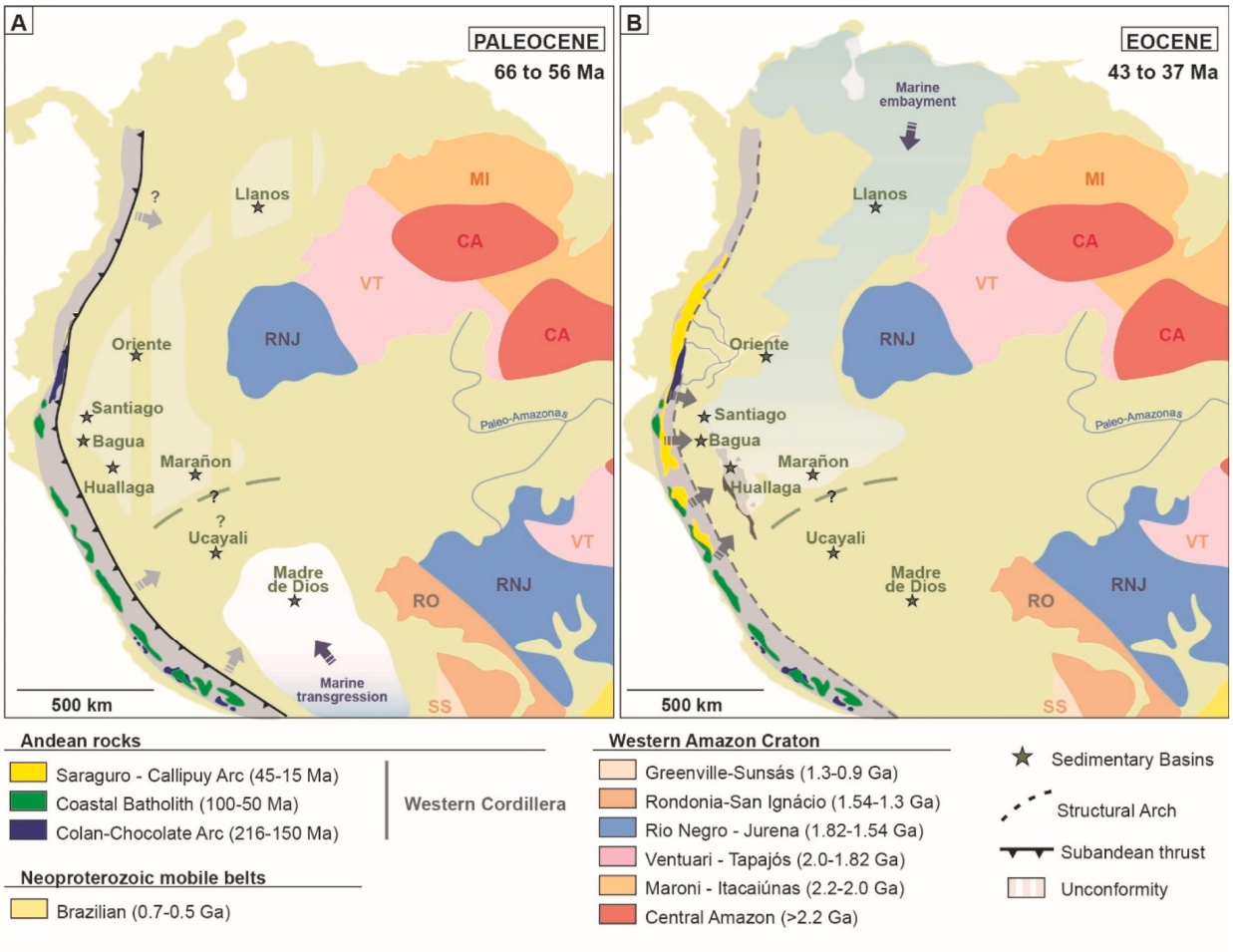


**Fig. 11.** Paleogeographic maps of Western Amazonia in Paleocene (A) Eocene (B) times. A) During the Paleocene, the northern part of the Western Amazonian basins are characterized by the presence of a regional unconformity while the southern part experienced shallow marine transgression (Louterbach et al., 2014). B) During the Eocene, the northern part likely experienced shallow marine embayment during short time-intervals through a connection with the Caribbean Sea while the southern part (the Madre de Dios Basin) is characterized by the absence of Eocene deposits (Louterbach et al., 2014).

CRediT authorship contribution statement

**Michele Andriolli Custódio:** Writing – original draft, Software, Methodology, Investigation, Funding acquisition, Formal analysis, Conceptualization. **Martin Roddaz:** Writing – original draft, Visualization, Validation, Supervision, Methodology, Investigation, Funding acquisition, Formal analysis, Data curation, Conceptualization. **Roberto Ventura Santos:** Writing – original draft, Visualization, Validation, Supervision, Resources, Project administration, Methodology, Investigation, Funding acquisition, Formal analysis, Conceptualization. **Pierre- Olivier Antoine:** Writing – original draft, Visualization, Validation, Resources, Methodology, Investigation, Funding acquisition, Formal analysis, Data curation. **Laurent Marivaux:** Writing – original draft, Visualization, Validation, Methodology, Investigation, Formal analysis, Data curation. **Narla S. Stutz:** Writing – original draft, Visualization, Methodology, Investigation, Funding acquisition, Formal analysis. **Elton Luiz Dantas:** Writing – original draft, Visualization, Validation, Resources, Methodology, Investigation, Funding acquisition, Formal analysis. **Carlos Jaramillo:** Writing – original draft, Visualization, Validation, Methodology, Investigation, Funding acquisition, Formal analysis. **Mélanie Louterbach:** Writing – review & editing, Visualization, Methodology, Investigation, Funding acquisition, Formal analysis. **Christian Hurtado:** Writing – original draft, Visualization, Validation, Methodology, Investigation, Funding acquisition, Formal analysis. **Guilherme de Oliveira Gonçalves:** Writing – original draft, Visualization, Validation, Software, Methodology, Formal analysis, Data curation.

Declaration of competing interest

The authors declare that they have no known competing financial interests or personal relationships that could have appeared to influence the work reported in this paper.

Data availability

Data will be made available on request.

## Acknowledgments

This work received financial and institutional support from the IRD (*Institut pour la Recherche et le Développement*). This study was also supported and funded by CAPES-COFECUB program Te 924/18/ 88881.143095/2017–01 "Paléo-Amazone: evolution Néogène de l'Amazonie Brésilienne/O PALEO AMAZONAS: evolução neogênica da Amazônia Brasileira", and CNPq (Proc. 312941/2018–8) "Neogene Evolution of Brazilian Amazon". This work was supported by an "Investissements d'Avenir" grant managed by the *Agence Nationale de la Recherche* (CEBA, ANR-10-LABX-25-01) and by the cooperative programs ECOS-FonCyT (A14-U01) and CoopIntEER CNRS-CONICET (n°252540), in the frame of the ongoing cooperation agreement between the *Museo de Historia Natural de la Universidad Nacional Mayor San Marcos* (Lima, Peru) and the *Institut des Sciences de l'Évolution-Université de Montpellier*. We thank two anonymous reviewers as well as the editor Michelangelo Martini for valuable reviews that improved this contribution.

### Appendix A. Supplementary data

Supplementary data to this article can be found online at:
https://doi. org/10.1016/j.jsames.2023.104256.

## References


Albert, J.S., Val, P., Hoorn, C., 2018. The changing course of the Amazon River in the Neogene: center stage for Neotropical diversification. Neotrop. Ichthyol. 16, 1–24. https://doi.org/10.1590/1982-0224-20180033.

Allen, P.A., Homewood, P., 1984. Evolution and mechanics of a Miocene tidal sandwave. Sedimentology 31, 63–81.

Alvim, A.M.V., Santos, R.V., Roddaz, M., Antoine, P.-O., Ramos, M.I.F., do Carmo, D.A., et al., 2021. Fossil isotopic constraints (C, O and 87Sr/86Sr) on Miocene shallow-marine incursions in Amazonia. Palaeogeogr. Palaeoclimatol. Palaeoecol. 573 https://doi.org/10.1016/j.palaeo.2021.110422.

Antoine, P.-O., Abello, M.A., Adnet, S., Altamirano Sierra, A.J., Baby, P., Billet, G., et al., 2016. A 60-million-year Cenozoic history of western Amazonian ecosystems in Contamana, eastern Peru. Gondwana Res. 31, 30–59. https://doi.org/10.1016/j. gr.2015.11.001.

Baby, P., Rivadeneira, M., Barragán, R., Christophoul, F., 2013. Thick-skinned tectonics in the Oriente foreland basin of Ecuador. In: Nemčok, M., Mora, A., Cosgrove, J.W. (Eds.), Thick-Skin-Dominated Orogens: from Initial Inversion to Full Accretion, vol. 377. Geological Society, London, Special Publications, pp. 59–76.

Baby, P., Calderón, Y., Brusset, S., Roddaz, M., Brichau, S., Eude, A., et al., 2018. The Peruvian sub-Andean foreland Basin system: structural overview, geochronologic constraints, and unexplored plays. AAPG Mem 117, 91–119. https://doi.org/10.1306/13622118M1173767.

Bahlburg, H., Vervoort, J.D., Du Frane, S.A., Bock, B., Augustsson, C., Reimann, C., 2009. Timing of crust formation and recycling in accretionary orogens: insights learned from the western margin of South America. Earth Science Reviews 97, 215–241. https://doi.org/10.1016/j.earscirev.2009.10.006.

Bayona, G., Baquero, M., Ramirez, C., Tabares, M., Salazar, A.F., Nova, G., Duarte, E., Pardo, A., Plata, A., Jaramillo, C., Rodriguez, G., Caballero, V., Cardona, A., Montes, C., Gomez-Marulanda, S., Cardenas-Rozo, A., 2021. Unraveling the widening of the earliest Andean northern orogen: Maastrichtian to early Eocene intra-basinal deformation in the northern Eastern Cordillera of Colombia. Basin Res. 33, 809–845.

Boonstra, M., Ramos, M.I.F., Lammertsma, E.I., Antoine, P.-O., Hoorn, C., 2015. Marine connections of Amazonia: evidence from foraminifera and dinoflagellate cysts (early to middle Miocene, Colombia/Peru). Palaeogeogr. Palaeoclimatol. Palaeoecol. 417, 176–194. https://doi.org/10.1016/j.palaeo.2014.10.032.

Bühn, B., Pimentel, M.M., Matteini, M., Dantas, E.L., 2009. High spatial resolution analysis of Pb and U isotopes for geochronology by laser ablation multi-collector inductively coupled plasma mass spectrometry (LA-MC-ICP-MS). An. Acad. Bras. Cienc. 81, 99–114. https://doi.org/10.1590/s0001-37652009000100011.

Burne, R.V., Bauld, J., De Deckker, P., 1980. Saline Lake Charophytes and Their Geological Significance. J. Sed. Petrol. 50 (1), 281–293. https://doi.org/10.1306/212F79D2-2B24-11D7-8648000102C1865D.

Caballero, V.-M., Naranjo, J.-F., Rodriguez, G., Gomez, P.-D., Mora, A., Villamizar, C., Miller, F., Gélvez, J., 2020. Eocene facies successions and environments in the southern Llanos Basin, Colombia. Ciencia, Tecnologia y Futuro 10, 107–122. Num 1.

Calderón, Y., Baby, P., Hurtado, C., Brusset, S., 2017a. Thrust tectonics in the Andean retro-foreland Basin of northern Peru: Permian inheritances and petroleum implications. Mar. Petrol. Geol. 82, 238–250. https://doi.org/10.1016/j.marpetgeo.2017.02.009.

Calderón, Y., Vela, Y., Hurtado, C., Bolaños, R., Baby, P., Eude, A., et al., 2017b. Petroleum systems restoration of the Huallaga-Marañon Andean retroforeland basin, Peru. AAPG Mem 114, 95–116. https://doi.org/10.1306/13602026M1143702.

Cappetta, H., Gayet, M., 2013. A new elasmobranch genus (Myliobatiformes, Dasyatoidea) from the Danian of Potosí (Bolivia). Neues Jahrbuch Geol. Palaontol. Abhand. 269, 285–290. https://doi.org/10.1127/0077-7749/2013/0351.

Carrillo, E., Barragán, R., Hurtado, C., Calderón, Y., Martín, G., Vázquez-Taset, Y., Parra, M., Rivera, A., Cadena, F.M., Sarmiento, L., 2021. Depositional sequences in northern Peru: new insights on the palaeogeographic and palaeotectonic reconstruction of western Gondwana during late Permian and Triassic. J. Geol. Soc. 178 (6), jgs2020–j2186. https://doi.org/10.1144/jgs2020-186, 2021.

Carvalho, M.R., Jaramillo, C., De la Parra, F., Caballero-Rodriguez, D., Herrera, F., Wing, S., Turner, B.L., D'Apolito, C., Romero-Baez, M., Narváez, P., Martinez, C., Gutierrez, M., Labandeira, C., Bayona, G., Rueda, M., Paez-Reyes,

M., Cardenas, D., Duque, A., Crowley, J.L., Santos, C., Silvestro, D., 2021. Extinction at the end- Cretaceous and the origin of modern Neotropical rainforests. Science 372, 63–68.

Chew, D.M., Magna, T., Kirkland, C.L., Mišković, A., Cardona, A., Spikings, R., Schaltegger, U., 2008. Detrital zircon fingerprint of the Proto-Andes: evidence for a Neoproterozoic active margin? Precambrian Research 167, 186–200. https://doi.or g/10.1016/j.precamres.2008.08.002.

Christophoul, F., Baby, P., Dávila, C., 2002. Stratigraphic responses to a major tectonic event in a foreland basin: the Ecuadorian Oriente Basin from Eocene to Oligocene times. Tectonophysics 345, 281–298. https://doi.org/10.1016/S0040-1951(01)00217-7.

Collinson, J.D., 1996. Alluvial sediments. In: Reading, H.G. (Ed.), Sedimentary Environments: Processes, Facies and Stratigraphy, third ed. Blackwell Science, Oxford, pp. 37–81.

Dalrymple, R.W., 1984. Morphology and internal structure of sand waves in the Bay of Fundy. Sedimentology 31, 365–382.

Dalrymple, R.W., Choi, K.S., 2003. Sediment transport by tidal currents. In: Middleton, G.V. (Ed.), Encyclopedia of Sediments and Sedimentary Rocks. Kluwer Academic.

Dalrymple, R.W., Choi, K.S., 2007. Morphologic and facies trends through the fluvial/marine transition in tide-dominated depositional systems: a schematic framework for environmental and sequence-stratigraphic interpretation. Earth Sci. Rev. 81, 135–174.

Dalrymple, R.W., Zaitlin, B.A., Boyd, R., 1992. Estuarine facies models: conceptual basis and stratigraphic implications. J. Sediment. Petrol. 62 (No. 6), 1130–1146.

Dashtgard, S.E., Gingras, M.K., 2012. Chapter 10: marine invertebrate neoichnology. In: Knaust, D., Bromley, R.G. (Eds.), Trace Fossils as Indicators of Sedimentary Environments. Elsevier, New York, pp. 273–295.

De La Parra, F., Pinzon, D., Mantilla-Duran, F., Rodriguez, G., Caballero, V., 2021. Marine-lacustrine systems during the Eocene in northern South America – palynological evidence from Colombia. J. South Am. Earth Sci. 108, 103188 https:// doi.org/10.1016/j.jsames.2021.103188.

DeCelles, P.G., Giles, K.A., 1996. Foreland Basin systems. Basin Res. 8, 105–123. https:// doi.org/10.1046/j.1365-2117.1996.01491.x.

Dickinson, W.R., Gehrels, G.E., 2009. Use of U-Pb ages of detrital zircons to infer maximum depositional ages of strata: a test against a Colorado Plateau Mesozoic database. Earth Planet Sci. Lett. 288, 115–125. https://doi.org/10.1016/j. epsl.2009.09.013.

Dunham, R.J., 1962. Classification of carbonate rocks according to depositional texture. In: Ham, W.E. (Ed.), Classification of Carbonate Rocks. AAPG, Tulsa, pp. 108–121.

Eakin, C.M., Lithgow-Bertelloni, C., Dávila, F.M., 2014. Influence of Peruvian flat-subduction dynamics on the evolution of western Amazonia. Earth Planet Sci. Lett. 404, 250–260. https://doi.org/10.1016/j.epsl.2014.07.027.

Espurt, N., Baby, P., Brusset, S., Roddaz, M., Hermoza, W., Regard, V., et al., 2007. How does the Nazca Ridge subduction influence the modern Amazonian foreland Basin? Geology 35, 515–518. https://doi.org/10.1130/G23237A.1.

Espurt, N., Baby, P., Brusset, S., Roddaz, M., Hermoza, W., Barbarand, J., 2010. The Nazca ridge and uplift of the Fitzcarrald Arch: implications for regional geology in northern South America. Amazon. Landsc. Species Evol. Look Past 89–100. https:// doi.org/10.1002/9781444306408.ch6.

Eude, A., Roddaz, M., Brichau, S., Brusset, S., Calderon, Y., Baby, P., et al., 2015. Controls on timing of exhumation and deformation in the northern Peruvian eastern Andean wedge as inferred from low-temperature thermochronology and balanced cross section. Tectonics 34, 715–730. https://doi.org/10.1002/2014TC003641.

Figueiredo, J., Hoorn, C., van der Ven, P., Soares, E., 2009. Late Miocene onset of the Amazon River and the Amazon deep-sea fan: evidence from the foz do Amazonas Basin. Geology 37, 619–622. https://doi.org/10.1130/G25567A.1.

Flemming, B.W., 2012. Siliciclastic back-barrier tidal flats. In: Davis Jr., R., Dalrymple, R. (Eds.), Principles of Tidal Sedimentology. Springer, Dordrecht. https://doi.org/ 10.1007/978-94-007-0123-6_10.

Flügel, E., 2010. In: Munnecke, A. (Ed.), Microfacies of Carbonates Rocks - Analysis,

Galbraith, R.F., 2005. Statistics for Fission Track Analysis. CRC Press.

Galbraith, R., Laslett, G., 1993. Statistical models for mixed fission track ages. Nucl. Tracks Radiat. Meas. 21 (4), 459–

470.
Gayet, M., Meunier, F.J., Werner, C., 2002. Diversification in Polypteriformes and special comparison with the Lepisosteiformes. Palaeontology 45 (2), 361–376.
Gehrels, G., 2014. Detrital zircon U-Pb geochronology applied to tectonics. Annu. Rev. Earth Planet Sci. 42, 127–149. https://doi.org/10.1146/annurev-earth-050212-124012.
Gehrels, G.E., Valencia, V.A., Ruiz, J., 2008. Enhanced precision, accuracy, efficiency, and spatial resolution of U-Pb ages by laser ablation-multicollector-inductively coupled plasma-mass spectrometry. G-cubed 9, 1–13. https://doi.org/10.1029/ 2007GC001805.
George, S.W.M., Horton, B.K., Jackson, L.J., Moreno, F., Carlotto, V., Garzione, C.N., 2019. Sediment provenance variations during contrasting Mesozoic-early Cenozoic tectonic regimes of the northern Peruvian Andes and Santiago-Marañón foreland Basin. https://doi.org/10.1016/b978-0-12-816009-1.00012-5.
Gorini, C., Haq, B.U., dos Reis, A.T., Silva, C.G., Cruz, A., Soares, E., et al., 2014. Late Neogene sequence stratigraphic evolution of the foz do Amazonas Basin, Brazil. Terra. Nova 26, 179–185. https://doi.org/10.1111/ter.12083.
Guiguer, K.R.R.A., Drimmie, R., Power, M., 2003. Validating methods for measuring d18O and d13C in otoliths from freshwater fish. Rapid Commun. Mass Spectrom. 17, 463–471, 2003.
Gutierrez, M., 1982. Evaluación potential petrolífero cuencas Huallaga, Ucayali y Madre de Dios. Zonación bioestratigráfica del intervalo Cretáceo superior-Terciario inferior. Petroperú. Rapport interne inédit, Lima, p. 29.
Gutiérrez, E.G., Horton, B.K., Vallejo, C., Jackson, L.J., George, S.W.M., 2019. Provenance and geochronological insights into late cretaceous-cenozoic foreland basin development in the subandean zone and Oriente Basin of Ecuador. In: Horton, B.K., Folguera, A. (Eds.), Andean Tectonics. Elsevier, pp. 237–268. https:// doi.org/10.1016/B978-0-12-816009-1.00011-3.
Hermoza, W., 2004. Dynamique tectono-sédimentaire et restauration séquentielle du rétro-bassin d'avant-pays des Andes centrales. Available at: http://www.theses.fr. (Accessed 10 January 2022) http://www.theses.fr/2004TOU30134. Accessed.
Hermoza, W., Brusset, S., Baby, P., Gil, W., Roddaz, M., Guerrero, N., et al., 2005. The Huallaga foreland Basin evolution: thrust propagation in a deltaic environment, northern Peruvian Andes. J. South Am. Earth Sci. 19, 21–34. https://doi.org/ 10.1016/j.jsames.2004.06.005.
Hoorn, C., 1993. Marine incursions and the influence of Andean tectonics on the Miocene depositional history of northwestern Amazonia: results of a palynostratigraphic study. Palaeogeogr. Palaeoclimatol. Palaeoecol. 105, 267–309. https://doi.org/ 10.1016/0031-0182(93)90087-Y.
Hoorn, C., Wesselingh, F.P., Hovikoski, J., Guerrero, J., 2010a. The development of the Amazonian mega-wetland (Miocene; Brazil, Colombia, Peru, Bolivia). Amazon. Landsc. Species Evol. Look Past 123–142. https://doi.org/10.1002/9781444306408.ch8.
Hoorn, C., Wesselingh, F.P., Ter Steege, H., Bermudez, M.A., Mora, A., Sevink, J., et al., 2010b. Amazonia through time: Andean uplift, climate change, landscape evolution, and biodiversity. Science 330, 927–931. https://doi.org/10.1126/science.1194585.
Hoorn, C., Bogotá-A, G.R., Romero-Baez, M., Lammertsma, E.I., Flantua, S.G.A., Dantas, E.L., et al., 2017. The Amazon at sea: onset and stages of the Amazon River from a marine record, with special reference to Neogene plant turnover in the drainage Basin. Global Planet. Change 153, 51–65. https://doi.org/10.1016/j. gloplacha.2017.02.005.
Horton, B.K., 2018. Sedimentary record of Andean mountain building. Earth Sci. Rev. 178, 279–309. https://doi.org/10.1016/j.earscirev.2017.11.025.
Horton, B.K., 2022. Unconformity development in retroarc foreland basins: implications for the geodynamics of Andean-type margins. J. Geol. Soc. 179.
Hovikoski, J., Wesselingh, F.P., Räsänen, M., Gingras, M., Vonhof, H.B., Marine influence in Amazonia: evidence from the geological record, 2010. In: Hoorn, C., Wesselingh, F.P. (Eds.), Amazonia, Landscape and Species Evolution. Blackwell Publishing), pp. 143–161.
Hurtado, C., Roddaz, M., Santos, R.V., Baby, P., Antoine, P.-O., Dantas, E.L., 2018. Cretaceous-early Paleocene drainage shift of Amazonian rivers driven by Equatorial Atlantic Ocean opening and Andean uplift as deduced from the provenance of northern Peruvian sedimentary rocks (Huallaga Basin). Gondwana Res.

63, 152–168. https://doi.org/10.1016/j.gr.2018.05.012.
Ingram, B.L., Conrad, M.E., Ingle, J.C., 1996. Stable isotope and salinity systematics in estuarine waters and carbonates: San Francisco Bay. Geochem. Cosmochim. Acta 60, 455–467. https://doi.org/10.1016/0016-7037(95)00398-3.
Jackson, S.E., Pearson, N.J., Griffin, W.L., Belousova, E., 2004. The application of laser ablation inductively coupled plasma mass spectrometry to in-situ U–Pb zircon geochronology. Chem. Geol. 211, 47–69.
Jaillard, E., Bengtson, P., Dhondt, A.V., 2005. Late Cretaceous marine transgressions in Ecuador and northern Peru: a refined stratigraphic framework. J. South Am. Earth Sci. 19, 307–323. https://doi.org/10.1016/j.jsames.2005.01.006.
Jaramillo, C., Rueda, M., 2021. A Morphological Electronic Database of Cretaceous-Tertiary Fossil Pollen and Spores from Northern South America V. 2012-2021. Smithsonian Tropical Research Institute. http://biogeodb.stri.si.edu/jaramillo/palynomorph/.
Jaramillo, C., Rueda, M., Torres, V., 2011. A palynological zonation for the Cenozoic of the Llanos and Llanos foothills of Colombia. Palynology 35, 46–84.
Jaramillo, C., Romero, I., D'Apolito, C., Bayona, G., Duarte, E., Louwye, S., et al., 2017. Miocene flooding events of western Amazonia. Sci. Adv. 3, 1–12. https://doi.org/ 10.1126/sciadv.1601693.
Johnson, S.T., Dashtgard, S.E., 2014. Inclined heterolithic stratification in a mixed tidal–fluvial channel: differentiating tidal versus fluvial controls on sedimentation. Sediment. Geol. 301, 41–53.
Keith, M.L., Anderson, G.M., Eichler, R., 1964. Carbon and oxygen isotopic composition of mollusk shells from marine and fresh-water environments. Geochem. Cosmochim. Acta 28, 1757–1786. https://doi.org/10.1016/0016-7037(64)90021-3.
Klein, G. de V., 1970. Depositional and dispersal dynamics of intertidal sand bars. J. Sediment. Petrol. 40, 1095–1127.
Kummel, B., 1948. Geological reconnaissance of the Contamana region, Peru. Geol. Soc. Am. Bull. 12, 1217–1266. https://doi.org/10.1130/0016-7606, 1948)59.
Logvina, E., Mazurenko, L., Prasolov, E., 2004. Isotopic composition of carbon-13 and oxygen-18 from authigenic carbonates. In: Black Sea Region. AGU Spring Meeting Abstracts.
Longhitano, S.G., Mellere, D., Steel, R.J., Ainsworth, R.B., 2012. Tidal depositional systems in the rock record: a review and new insights. Sediment. Geol. 279, 2–22. https://doi.org/10.1016/j.sedgeo.2012.03.024.
Louterbach, M., Roddaz, M., Bailleul, J., Antoine, P.-O., Adnet, S., Kim, J.H., et al., 2014. Evidences for a Paleocene marine incursion in southern Amazonia (Madre de Dios sub-Andean zone, Peru). Palaeogeogr. Palaeoclimatol. Palaeoecol. 414, 451–471. https://doi.org/10.1016/j.palaeo.2014.09.027.
Louterbach, M., Fernández, O., Sisinni, V., Gutierrez, M., Zamora, G., 2018a. Stratigraphy, structure, and hydrocarbon potential of the northern Bolivia sub- Andean thrust belt (Beni basin). In: Petroleum Basins and Hydrocarbon Potential of the Andes of Peru and Bolivia AAPG Memoirs. AAPG), pp. 377–413.
Louterbach, M., Roddaz, M., Antoine, P.-O., Marivaux, L., Adnet, S., Bailleul, J., et al., 2018b. Provenance record of late Maastrichtian–late Palaeocene Andean mountain building in the Amazonian retroarc foreland basin (Madre de Dios basin, Peru). Terra. Nova 30, 17–23. https://doi.org/10.1111/ter.12303.
Miall, A.D., 1978. Lithofacies types and vertical profile models in braided river deposits: a summary. Fluv. Sedimentol. 5, 597–600.
Miall, A.D., 1996. The Geology of Fluvial Deposits, Sedimentary Facies, Basin Analysis and Petroleum Geology. Springer, Berlin.
Miall, A.D., 2006. The Geology of Fluvial Deposits. https://doi.org/10.1007/978-3-662- 03237-4.
Moreno, F., Garzione, C.N., George, S.W.M., Horton, B.K., Williams, L., Jackson, L.J., et al., 2020. Coupled Andean growth and foreland basin evolution, Campanian–Cenozoic Bagua Basin, northern Peru. Tectonics 39. https://doi.org/ 10.1029/2019TC005967.
Moreno, F., Garzione, C.N., George, S.W.M., Williams, L., Richter, F., Bandeian, A., 2022. Late cretaceous through Cenozoic paleoenvironmental history of the Bagua Basin, Peru: paleoelevation comparisons with the central Andean plateau. Geosciences 12, 242. https://doi.org/10.3390/geosciences12060242.
Mowbray, T. and Visser, M. J. 1984. Reactivation surfaces in subtidal channel deposits, Oosterschelde, Southwest Netherlands. Journal of Sedimentary Research; 54 (3): 811–824. https://doi.org/10.1306/212F8503-2B24-11D7-8648000102C1865D.

Naeser, C.W., Crochet, J.Y., Jaillard, E., Laubacher, G., Mourier, T., Sigé, B., 1991. Tertiary fission-track ages from the Bagua syncline (northern Peru): stratigraphic and tectonic implications. J. South Am. Earth Sci. 4, 61–71. https://doi.org/ 10.1016/0895-9811(91)90018-G.

Nichols, G., 2009. Sedimentology and Stratigraphy, second ed. second ed. Wiley- Blackwell.

Odoh, S., Saylor, J.E., Higuera, C., Copeland, P., Lapen, T.J., 2019. Chapter 6: discriminating mechanisms for coarse clastic progradation in the Colombian foreland Basin using detrital zircon double dating. In: Horton, B.K., Folguera, A. (Eds.), Andean Tectonics. Elsevier, pp. 133–171. https://doi.org/10.1016/B978-0- 12-816009-1.00008-3.

Paton, C., Hellstrom, J., Paul, B., Woodhead, J., Hergt, J., 2011. Iolite: freeware for the visualisation and processing of mass spectrometric data. J. Anal. At. Spectrom. 26, 2508–2518. https://doi.org/10.1039/c1ja10172b.

Petrus, J.A., Kamber, B.S., 2012. VizualAge: a novel approach to laser ablation ICP-ms U- Pb geochronology data resolution. Geostand. Geoanal. Res. 36 (3), 247–270.

Platt, N.H., Wright, V.P., 1991. Lacustrine carbonates: facies models, facies distributions and hydrocarbon aspects. In: Anado´n, P., Cabrera, L., Kelts, K. (Eds.), Lacustrine Facies Analysis, vol. 13. International Association of Sedimentologists, Special Publication, pp. 57–74.

Reimann, C.R., Bahlburg, H., Kooijman, E., Berndt, J., Gerdes, A., Carlotto, V., Lopez, S., 2010. Geodynamic evolution of the early Paleozoic Western Gondwana margin 14°- 17°S reflected by the detritus of the Devonian and Ordovician basins of southern Peru and northern Bolivia. Gondwana Research 18, 370–384.

Roddaz, M., Baby, P., Brusset, S., Hermoza, W., Darrozes, J.M., 2005a. Forebulge dynamics and environmental control in Western Amazonia: the case study of the Arch of Iquitos (Peru). Tectonophysics 399, 87–108. https://doi.org/10.1016/j. tecto.2004.12.017.

Roddaz, M., Viers, J., Brusset, S., Baby, P., Hérail, G., 2005b. Sediment provenances and drainage evolution of the Neogene Amazonian foreland Basin. Earth Planet Sci. Lett. 239, 57–78. https://doi.org/10.1016/j.epsl.2005.08.007.

Roddaz, M., Hermoza, W., Mora, A., Baby, P., Parra, M., Christophoul, F., et al., 2010. Cenozoic sedimentary evolution of the Amazonian foreland basin system. Amazon. Landsc. Species Evol. Look Past 61–88. https://doi.org/10.1002/9781444306408. ch5.

Sacek, V., 2014. Drainage reversal of the Amazon River due to the coupling of surface and lithospheric processes. Earth Planet Sci. Lett. 401, 301–312. https://doi.org/ 10.1016/j.epsl.2014.06.022.

Santos, C., Jaramillo, C., Bayona, G., Rueda, M., Torres, V., 2008. Late Eocene marine incursion in north-western South America. Palaeogeogr. Palaeoclimatol. Palaeoecol. 264, 140–146. https://doi.org/10.1016/j.palaeo.2008.04.010.

Sempere, T., Butler, R.F., Richards, D.R., Marshall, L.G., Sharp, W., Swisher, C.C., 1997. Stratigraphy and chronology of upper Cretaceous-lower Paleogene strata in Bolivia and northwest Argentina. Bull. Geol. Soc. Am. 109, 709–727. https://doi.org/ 10.1130/0016-7606.

Sharman, G.R., Malkowski, M.A., 2020. Needles in a haystack: detrital zircon U-Pb ages and the maximum depositional age of modern global sediment. Earth Sci. Rev. 203, 103–109. https://doi.org/10.1016/j.earscirev.2020.103109.

Sharman, G.R., Sharman, J.P., Sylvester, Z., 2018. detritalPy: a Python-based toolset for visualizing and analysing detrital geo-thermochronologic data. Depositional Rec 4, 202–215. https://doi.org/10.1002/dep2.45.

Shephard, G.E., Müller, R.D., Liu, L., Gurnis, M., 2010. Miocene drainage reversal of the Amazon River driven by plate-mantle interaction. Nat. Geosci. 3, 870–875. https:// doi.org/10.1038/ngeo1017.

Thomas, R.G., Smith, D.G., Wood, J.M., Visser, J., Calverley-Range, E.A., Koster, E.H., 1987. Inclined heterolithic stratification-terminology, description, interpretation and significance. Sediment. Geol. 53, 123–179.

Traverse, A., 2007. Paleopalynology, second ed. Springer, Dordrecht, p. 813.

Tucker, M.E., Wright, P.V., 1990. Carbonate Sedimentology. Blackwell Science.

van Soelen, E.E., Kim, J.H., Santos, R.V., Dantas, E.L., Vasconcelos de Almeida, F., Pires, J.P., et al., 2017. A 30 Ma history of the Amazon River inferred from terrigenous sediments and organic matter on the Ceará Rise. Earth Planet Sci. Lett. 474, 40–48. https://doi.org/10.1016/j.epsl.2017.06.025.

Varol, B., 2015. Stable isotopes (d18O, d13C) of mollusk shells in environmental interpretations; an example from sinop Miocene succession (northern Turkey). Miner. Res Expl Bull 128, 49–60.

https://doi.org/10.19111/bmre.26386.
Vermeesch, P., 2018. IsoplotR: a free and open toolbox for geochronology. Geosci. Front. 9, 1479–1493.
Vermeesch, P., 2021. Maximum depositional age estimation revisited. Geosci. Front. 12, 843–850. https://doi.org/10.1016/j.gsf.2020.08.008.
Visser, M.J., 1980. Neap-spring cycles reflected in Holocene subtidal large-scale bedform deposits: a preliminary note. Geology 8, 543–546.
Vonhof, H.B., Wesselingh, F.P., Ganssen, G.M., 1998. Reconstruction of the Miocene Western Amazonian aquatic system using moluscan isotopes signatures. Palaeogeogr. Palaeoclimatol. Palaeoecol. 141, 85–93.
Walker, R.G., 1992. Facies, facies models and modern stratigraphic concepts. In: Walker, R.G., James, N.P. (Eds.), Facies Models: Response to Sea-Level Change. Geological Association of Canada, Toronto, pp. 1–14.
Wiedenbeck, M., Allé, P., Corfu, F., Griffin, W.L., Meier, M., Oberli, F., Von Quadt, A., Roddick, J.C., Spiegel, W., 1995. Three natural zircon standards for U-Th-Pb.Lu-Hf, trace element and REE analyses. Geostandards 1950 Newsletter 19, 1–23.
Zamora, G., Gil, W., 2018. The Marañón Basin: tectonic evolution and paleogeography. AAPG Mem 117, 121–143. https://doi.org/10.1306/13622119M1173768.
Zapata, S., Zapata-Henao, M., Cardona, A., Jaramillo, C., Silvestro, D., Oboh-Ikuenobe, F., 2021. Long-term topographic growth and decay constrained by 3D thermo-kinematic modeling: tectonic evolution of the Antioquia Altiplano, Northern Andes. Glob Planet. Change 203, 103553.
Calvès, G., Calderón, Y., Hurtado, C., Brusset, S., Santini, W., Baby, P. 2018. Mass Balance of Cenozoic Andes-Amazon Source to Sink System-Marañón Basin, Peru. Geosciences, MDPI, 8 (5). f10.3390/geosciences8050167ff.ffhal-01787548f.